Magneto-elastic oscillations of neutron stars: exploring different magnetic field configurations

Michael Gabler[1,2], Pablo Cerdá-Durán[1], José A. Font[1], Ewald Müller[2]
and Nikolaos Stergioulas[3]

[1] *Departamento de Astronomía y Astrofísica, Universidad de Valencia, 46100 Burjassot (Valencia), Spain*
[2] *Max-Planck-Institut für Astrophysik, Karl-Schwarzschild-Str. 1, 85741 Garching, Germany*
[3] *Department of Physics, Aristotle University of Thessaloniki, Thessaloniki 54124, Greece*

28 February 2013

ABSTRACT

We study magneto-elastic oscillations of highly magnetized neutron stars (magnetars) which have been proposed as an explanation for the quasi-periodic oscillations (QPOs) appearing in the decaying tail of the giant flares of soft gamma-ray repeaters (SGRs). We extend previous studies by investigating various magnetic field configurations, computing the Alfvén spectrum in each case and performing magneto-elastic simulations for a selected number of models. By identifying the observed frequencies of 28 Hz (SGR 1900+14) and 30 Hz (SGR 1806-20) with the fundamental Alfvén QPOs, we estimate the required surface magnetic field strength. For the magnetic field configurations investigated (dipole-like poloidal, mixed toroidal-poloidal with a dipole-like poloidal component and a toroidal field confined to the region of field lines closing inside the star, and for poloidal fields with an additional quadrupole-like component) the estimated dipole spin-down magnetic fields are between 8×10^{14}G and 4×10^{15}G, in broad agreement with spin-down estimates for the SGR sources producing giant flares. A number of these models exhibit a rich Alfvén continuum revealing new turning points which can produce QPOs. This allows one to explain most of the observed QPO frequencies as associated with magneto-elastic QPOs. In particular, we construct a possible configuration with two turning points in the spectrum which can explain all observed QPOs of SGR 1900+14. Finally, we find that magnetic field configurations which are entirely confined in the crust (if the core is assumed to be a type I superconductor) are not favoured, due to difficulties in explaining the lowest observed QPO frequencies ($f \lesssim 30$ Hz).

1 INTRODUCTION

The discovery of quasi-periodic oscillations (QPOs) in the decaying tail of a giant flare of a soft-gamma ray repeater[1] (SGR) by Israel et al. (2005) (see also Watts & Strohmayer 2007, and references therein) has stimulated strong interest in the theoretical modelling of oscillations of magnetized neutron stars (magnetars). The observed frequencies of the QPOs are roughly 18, 26, 30, 92, 150, 625, and 1840 Hz for the outburst of SGR 1806-20 and 28, 53, 84, and 155 Hz for SGR 1900+14, respectively. Since the first attempts to explain these QPOs in terms of torsional, purely shear modes of the solid crust of the neutron star (Duncan 1998; Strohmayer & Watts 2005; Piro 2005; Sotani et al. 2007; Samuelsson & Andersson 2007; Steiner & Watts 2009) the theoretical understanding of the oscillations has evolved. The most recent studies (Gabler et al. 2011, 2012; Colaiuda & Kokkotas 2011; van Hoven & Levin 2011, 2012) favour global magneto-elastic oscillations as an explanation for the lower frequency ($f < 200$ Hz) QPOs. In these works the coupling through the magnetic field leads to a very efficient absorption of the shear modes of the crust into the core even for magnetic

field strengths well below those estimated for magnetars, $B_{15} \sim 1$ with $B_{15} \equiv B[10^{15}$ G] (Duncan & Thompson 1992). Nonetheless, long-lived QPOs which have predominantly Alfvén character have also been studied (Sotani et al. 2008; Cerdá-Durán et al. 2009; Colaiuda et al. 2009). The frequencies of successive overtones of these QPOs are found in integer relations and, thus, can potentially explain some of the observed frequency relations. In two previous papers (Gabler et al. 2011, 2012) we have shown that these oscillations can reach the surface of the star with significant amplitudes only for magnetic fields stronger than $B_{15} \gtrsim 1$, if the internal field has a global, dipole-like structure.

A successful interpretation of the observed QPOs has the potential to constrain the equation of state (EoS) of the cold matter at supranuclear densities which occur only in the core of a neutron star (Samuelsson & Andersson 2007). Therefore, neutron stars are a unique laboratory that can be used to increase our knowledge of the fundamental physics describing the interaction of nucleons and other elementary particles at the conditions inside those stars.

While the current models of magneto-elastic oscillations are promising to explain some of the observed QPO frequencies, all existing studies are restricted to a very limited set of magnetic field configurations. The aim of the present work is to explore the influence of the magnetic field configuration in the magneto-elastic

---

[1] SGRs are assumed to be highly magnetized neutron stars showing repeated bursts in the soft-gamma ray spectrum (Duncan & Thompson 1992)

model of QPOs to assess its validity. It must be stressed that very little is known from observations about the internal magnetic field configurations of magnetars. The only observational constraint is the presence of a strong external field which is responsible for the observed spin-down of the magnetar. Both purely toroidal and purely poloidal magnetic fields are known to be unstable in unstratified stars, i.e. stars with a barotropic EoS which depends on one parameter only (Tayler 1973; Markey & Tayler 1973). Nonlinear simulations confirm these instabilities (Braithwaite & Spruit 2006; Kiuchi et al. 2011; Ciolfi et al. 2011; Lasky et al. 2011; Lander & Jones 2011a,b) and suggest that a twisted torus configuration, with mixed poloidal and toroidal field, is expected. There have been some attempts to model magnetic field configurations as equilibrium axisymmetric configurations with mixed poloidal and toroidal field (Colaiuda et al. 2008; Kiuchi & Kotake 2008; Ciolfi et al. 2009; Lander & Jones 2009). However, no stable configuration has yet been found for barotropic stars (Lander & Jones 2012). Nevertheless, different possibilities could stabilize magnetic fields in stars: a more complicated magnetic field structure (possibly nonaxisymmetric), stratification, or the presence of a solid crust. Until this issue is settled, it is legitimate to explore the most general setup of magnetic field configurations possible and analyze their influence on the QPO frequencies, leaving aside the stability of the configurations. This paper, in which we explore a wide range of plausible axisymmetric magnetic field configurations, summarizes our findings in this direction.

We begin this paper in Section 2 with a short overview of our theoretical and numerical framework, described in more detail in Cerdá-Durán et al. (2009) and Gabler et al. (2012). We also describe in detail in this section how to obtain different magnetic field configurations with a new implementation of the MAGSTAR tool of the LORENE library which we call MAGNETSTAR. In the following sections we consider different magnetic field configurations, including dipole-like fields in Section 3 and quadrupole-like fields in Section 4, where mixed quadrupole-dipole-like fields are also considered. We further divide the dipole-like fields into purely poloidal fields (Section 3.1) and mixed toroidal-poloidal fields (Section 3.2). All magnetic field configurations considered up to Section 4 penetrate the whole volume of the star. In Section 5 we study the case of a magnetic field confined to the crustal region, a situation motivated by the indications that neutron stars may contain superconducting protons (Page et al. 2011; Shternin et al. 2011) in which case the magnetic field could be expelled from the core of the neutron star, if it is a type I superconductor. A summary of our results is presented in Section 7.

We use units where $c = G = 1$ with c and G being the speed of light and the gravitational constant, respectively. Latin (Greek) indices run from 1 to 3 (0 to 3). Partial and covariant derivatives are indicated by a comma and a semicolon, respectively. We apply the Einstein summation convention.

2   THEORETICAL FRAMEWORK

2.1   General-relativistic magneto-hydrodynamics of elastic bodies

In the present work we adopt the framework of 3+1 split of general relativity for a spherically-symmetric spacetime. The metric takes the following form

$$ds^2 = -\alpha^2 dt^2 + \Phi^4 \hat{\gamma}_{ij} dx^i dx^j \,, \tag{1}$$

where α is the lapse function, $\hat{\gamma}_{ij}$ is the flat, spatial three-metric, and Φ is the conformal factor.

The stress-energy tensor $T^{\mu\nu}$ for a magnetized perfect fluid with elastic properties can be written as a sum of different contributions:

$$
\begin{aligned}
T^{\mu\nu} &= T^{\mu\nu}_{\text{fluid}} + T^{\mu\nu}_{\text{magn}} + T^{\mu\nu}_{\text{elas}} \\[4pt]
&= \rho h u^\mu u^\nu + P g^{\mu\nu} + b^2 u^\mu u^\nu + \tfrac{1}{2} b^2 g^{\mu\nu} - b^\mu b^\nu \\[4pt]
&\quad - 2\mu_{\text{S}} \Sigma^{\mu\nu} \,,
\end{aligned}
\tag{2,3}
$$

where ρ is the rest-mass density, $h = 1 + \epsilon + p/\rho$ the specific enthalpy, ϵ the specific internal energy, P the isotropic fluid pressure, u^μ the four-velocity of the fluid and $g^{\mu\nu}$ the metric tensor. In the magnetic contribution to the stress-energy tensor we find the magnetic field b^μ, measured by a co-moving observer, with $b^2 = b_\mu b^\mu$, and in the elastic contribution we find the shear modulus μ_{S} and the shear tensor $\Sigma^{\mu\nu}$.

We are interested in torsional oscillations of neutron stars and are thus allowed to simplify the model as follows: (i) We use a *barotropic* EoS. (ii) For *poloidal* background fields and in *axisymmetry* the *axial oscillations* decouple at the *linear level* from the polar oscillations. With these assumptions, we evolve only B^φ and S_φ (see definitions below). (iii) We apply the *Cowling approximation*, regarding the metric as fixed. (iv) For torsional oscillations the shear tensor Σ^{ij} can be expressed as

$$
\Sigma^{ij} = \frac{1}{2}
\begin{bmatrix}
0 & 0 & g^{rr}\xi^\varphi_{,r} \\
0 & 0 & g^{\theta\theta}\xi^\varphi_{,\theta} \\
g^{rr}\xi^\varphi_{,r} & g^{\theta\theta}\xi^\varphi_{,\theta} & 0
\end{bmatrix},
\tag{4}
$$

while the other components vanish, $\Sigma^{\mu 0} = \Sigma^{0\nu} = 0$. Here, we have introduced the displacement ξ^i, which is defined via its time derivative as $\xi^i_{,t} = \alpha v^i$.

With these simplifications the conservation of energy and momentum $\nabla_\nu T^{\mu\nu} = 0$, baryon number conservation $\nabla_\nu(\rho u^\nu) = 0$, and the Maxwell's equations $\nabla_\nu {}^*F^{\mu\nu} = 0$ and $\nabla_\nu F^{\mu\nu} = 4\pi \mathcal{J}^\mu$ lead to the following flux-conservative hyperbolic system of equations

$$
\frac{1}{\sqrt{-g}} \left(\frac{\partial \sqrt{\gamma} \mathbf{U}}{\partial t} + \frac{\partial \sqrt{-g} \mathbf{F}^i}{\partial x^i} \right) = 0 \,.
\tag{5}
$$

The various quantities introduced here are the Faraday electromagnetic tensor field $F^{\mu\nu}$ and its dual ${}^*F^{\mu\nu}$, the electric current $\mathcal{J}^\mu$, $\sqrt{-g} = \alpha\sqrt{\gamma}$, and $\gamma = det(\gamma_{ij})$. The state vector $\mathbf{U}$ and the flux vector $\mathbf{F}^i$ are given by

$$
\mathbf{U} = [S_\varphi, B^\varphi],
\tag{6}
$$

$$
\mathbf{F}^r = \left[-\frac{b_\varphi B^r}{W} - 2\mu_{\text{S}}\Sigma^r_{\;\varphi}, -v^\varphi B^r \right],
\tag{7}
$$

$$
\mathbf{F}^\theta = \left[-\frac{b_\varphi B^\theta}{W} - 2\mu_{\text{S}}\Sigma^\theta_{\;\varphi}, -v^\varphi B^\theta \right],
\tag{8}
$$

where $W = \alpha u^t$ is the Lorentz factor, v^i is the three-velocity of the fluid, and $S_i = (\rho h + b^2)W^2 v_i - \alpha b_i b^0$ is a generalization of the momentum density. The relation between the magnetic field measured by an Eulerian observer, B^i, and b^i is given by

$$
b^\mu = \left[\frac{W B^i v_i}{\alpha}, \frac{B^i + W^2 v^j B_j \hat{v}^i}{W} \right].
\tag{9}
$$

Eq. (5) is complemented by the evolution equations of the displacement

$$
(\xi^\varphi_{,r})_{,t} - (v^\varphi \alpha)_{,r} = 0,
\tag{10}
$$

$$
(\xi^\varphi_{,\theta})_{,t} - (v^\varphi \alpha)_{,\theta} = 0.
\tag{11}
$$

Boundary conditions

The boundary and interface conditions have been discussed in Gabler et al. (2012). For brevity, here, we only state the conditions and refer the reader to the previous work for details. The different conditions are direct consequences of momentum conservation and the assumption of ideal MHD.

At the neutron star surface this leads to the continuous traction condition and the assumption that there are no surface currents. Therefore, the tangential magnetic field components have to be continuous, i.e. $b^{\varphi}_{\mathrm{crust}} = b^{\varphi}_{\mathrm{atmosphere}}$ at the surface and $\xi^{\varphi}_{\mathrm{crust},r} = 0$.

At the crust-core interface we have two separate cases: (i) If the magnetic field penetrates the core we can define a displacement at this interface as well and ξ^{φ} has to be continuous. As above, we use the continuity of the traction to set the remaining condition which then reads $\xi^{\varphi}_{\mathrm{core},r} = \left[1 + \mu_{\mathrm{S}}/\Phi^4(b^r)^2\right]\xi^{\varphi}_{\mathrm{crust},r}$. (ii) If the magnetic field is confined to the crust, the continuous traction condition leads to $\xi^{\varphi}_{\mathrm{crust},r} = 0$ at the crust-core interface, too.

Numerical methods

The numerical simulations are performed with the non-linear GRMHD code MCOCOA described in previous works (Cerdá-Durán et al. 2008, 2009; Gabler et al. 2012). This code is able to compute the torsional oscillations of neutron stars with strong magnetic fields and an elastic crust. To solve the GRMHD equations we employed a high-resolution shock-capturing scheme with a method of lines for the time-advance.

Complementary to the numerical simulations, we will also make use of the semi-analytic model presented in Cerdá-Durán et al. (2009), which allows us to compute the spectrum of standing-wave magneto-elastic oscillations along individual magnetic field lines. The model is based on an integration of a perturbation along the magnetic field lines in the limit of short wavelengths. We extended this method in Gabler et al. (2012) to approximately take into account the elastic crust.

Microphysics

We construct neutron star models choosing different combinations of EoS: the EoS APR (Akmal et al. 1998) or the stiffer EoS L (Pandharipande & Smith 1975) for the core, and EoS NV (Negele & Vautherin 1973) or EoS DH (Douchin & Haensel 2001) for the crust.

The calculation of the shear modulus μ_{S} is based on the zero-temperature limit of Strohmayer et al. (1991)

$$\mu_{\mathrm{S}} = 0.1194 \frac{n_i(Ze)^2}{a},\qquad(12)$$

where n_i is the ion density, Ze the ion charge, and $a^3 = 3/(4\pi n_i)$ the average ion spacing. For details see Gabler et al. (2012).

2.2 Magnetic equilibria

The hydrostatic equilibrium equations for a self-gravitating magnetized star (see Gourgoulhon 2012, and references therein) can be simplified under the following assumptions: (i) axisymmetry, (ii) no rotation or meridional flows, (iii) no net charges, (iv) a barotropic EoS of the form $P = P(\rho)$, and (v) an unstressed crust, $\Sigma^{\mu\nu} = 0$. These conditions are appropriate to describe magnetars, which are regarded to be cold and slowly rotating. In that case

$$(\log h + \log \alpha)_{,i} = \frac{1}{\rho h}\epsilon_{ijk}\mathcal{J}^j B^k,\qquad(13)$$

where $\mathcal{J}^i$ is the magnetic current. For the magnetic field strength relevant for magnetars, $B < 10^{16}$ G, deformations of the equilibrium configurations due to magnetic field stresses are small (Bocquet et al. 1995). Therefore, we can expand around the unmagnetized spherical equilibrium values, $h = h_0 + h'$ and $\alpha = \alpha_0 + \alpha'$, such that $h' \ll h_0$, $\alpha' \ll \alpha_0$, and

$$(\log h_0 + \log \alpha_0)_{,i} = 0.\qquad(14)$$

Neglecting magnetic terms in density and pressure terms the resulting equation for the linearized perturbations is

$$M_{,i} = \frac{1}{\rho_0 h_0}\epsilon_{ijk}\mathcal{J}^j B^k.\qquad(15)$$

where $M \equiv h'/h_0 + \alpha'/\alpha_0 \ll 1$, which quantifies the magnitude of the perturbation and can be used to assess the quality of the approximation. The equilibrium models presented later in this work do never exceed a maximum magnitude of $M \lesssim 5 \times 10^{-4}$. The current and the magnetic field are related by Ampere's law

$$\epsilon^{ijk}(\alpha B_k)_{,j} = 4\pi\alpha\mathcal{J}^i.\qquad(16)$$

Considering the restriction of the solenoidal condition for the magnetic field there are only two free functions describing the magnetic field configuration. For convenience we choose them to be $\tilde{H}_{\varphi} \equiv \alpha B_{\varphi}/4\pi$ and A_{φ}, the latter being the φ-component of the vector potential A_i defined as

$$B^i = \epsilon^{ijk}A_{k,j}.\qquad(17)$$

The equilibrium equations as a function of A_{φ} and $\tilde{H}_{\varphi}$ read

$$M_{,r} = \frac{1}{\rho_0 h_0}\left[\mathcal{J}^{\varphi}A_{\varphi,r} - \frac{4\pi\gamma^{\varphi\varphi}\tilde{H}_{\varphi}}{\alpha^2}\tilde{H}_{\varphi,r}\right]\qquad(18)$$

$$M_{,\theta} = \frac{1}{\rho_0 h_0}\left[\mathcal{J}^{\varphi}A_{\varphi,\theta} - \frac{4\pi\gamma^{\varphi\varphi}\tilde{H}_{\varphi}}{\alpha^2}\tilde{H}_{\varphi,\theta}\right]\qquad(19)$$

$$0 = A_{\varphi,r}\tilde{H}_{\varphi,\theta} - A_{\varphi,\theta}\tilde{H}_{\varphi,r}\qquad(20)$$

2.2.1 General magnetic field configurations

Eqs. (18-20) lead to four different branches of possible solutions for the current distribution:

• *Type I.- Mixed poloidal-toroidal current* ($\tilde{H}_{\varphi} = \tilde{H}_{\varphi}(A_{\varphi})$ *and* $d\tilde{H}_{\varphi}/dA_{\varphi} \neq 0$) generating a *mixed poloidal-toroidal field*: Eqs. (18-20) imply $M = M(A_{\varphi})$ and

$$\mathcal{J}^r = \frac{1}{\sqrt{-g}}\tilde{H}_{\varphi,\theta}$$

$$\mathcal{J}^{\theta} = -\frac{1}{\sqrt{-g}}\tilde{H}_{\varphi,r}$$

$$\mathcal{J}^{\varphi} = \rho_0 h_0\frac{dM}{dA_{\varphi}} + \frac{4\pi\gamma^{\varphi\varphi}}{\alpha^2}\tilde{H}_{\varphi}\frac{d\tilde{H}_{\varphi}}{dA_{\varphi}}.\qquad(21)$$

In this case we have two free functions $\tilde{H}_{\varphi}(A_{\varphi})$ and $M(A_{\varphi})$ to determine the current $\mathcal{J}^i(A_{\varphi})$, which in turn gives via the φ-component of Ampère's law A_{φ}. The solution of the system of equations is identical to that described in Bocquet et al. (1995). It generates a magnetic field with mixed poloidal and toroidal component. In the case $M = 0$, the configuration is force-free.

• *Type II.- Purely toroidal current* ($\tilde{H}_{\varphi} = 0$, $A_{\varphi} \neq 0$ *and* $\mathcal{J}_{\varphi} \neq 0$) generating a *purely poloidal field*: Eqs. (18-20) imply $M = M(A_{\varphi})$ and

$$\mathcal{J}^i = \left(0, 0, \rho_0 h_0 \frac{dM}{dA_\varphi}\right) \tag{22}$$

For a given form of $M(A_\varphi)$ and using $\mathcal{J}^\varphi$ in the φ-component of Ampere's law, Eq. (16), an elliptic system results that can be solved for A_φ. This is the procedure described by Bocquet et al. (1995) to compute self-consistent magnetic field equilibria, although their approach is more general since rotation, charges and the deformations of the star are considered, too. This configuration corresponds to a limiting case of the type I solution for $\tilde{H}_\varphi \to 0$.

• *Type III.- External currents ($\tilde{H}_\varphi = 0$, $\mathcal{J}^\varphi = 0$ and $A_\varphi \neq 0$) generating a force-free poloidal field*: Eqs. (18-20) imply $M = 0$, i.e. force-free poloidal configurations. It describes the magnetic field in regions with vanishing currents. The currents generating the magnetic field are external to the region described by this currents. The solution depends only on the potential A_φ that is a solution of:

$$\left(\frac{\alpha\gamma_{\theta\theta}}{\sqrt{\gamma}} A_{\varphi,r}\right)_{,r} + \left(\frac{\alpha\gamma_{rr}}{\sqrt{\gamma}} A_{\varphi,\theta}\right)_{,\theta} = 0. \tag{23}$$

This configuration corresponds to a limiting case of a type II current configuration with $\mathcal{J}^\varphi \to 0$.

• *Type IV.- Purely poloidal current ($A_\varphi = 0$ and $\tilde{H}_\varphi \neq 0$) generating a purely toroidal field*: Eqs. (18-20) imply $M = M(\tilde{H}_\varphi)$ and

$$\frac{dM}{d\tilde{H}_\varphi} = -\frac{4\pi\gamma^{\varphi\varphi}}{\rho_0 h_0 \alpha^2} \tilde{H}_\varphi. \tag{24}$$

For a given $M(\tilde{H}_\varphi)$, Eq. (24) provides the current and magnetic field configuration

$$\mathcal{J}^i = \left(\frac{1}{\sqrt{-g}} \tilde{H}_{\varphi,\theta}, -\frac{1}{\sqrt{-g}} \tilde{H}_{\varphi,r}, 0\right). \tag{25}$$

This current distribution generates a purely toroidal field confined to the region where $\mathcal{J}^i \neq 0$.

Once the current is known, and hence A_φ and $\tilde{H}_\varphi$, the magnetic field can be computed as

$$B^i = \left(\frac{1}{\sqrt{\gamma}} A_{\varphi,\theta}, -\frac{1}{\sqrt{\gamma}} A_{\varphi,r}, \frac{4\pi\gamma^{\varphi\varphi}}{\alpha} \tilde{H}_\varphi\right) \tag{26}$$

2.2.2 Magnetic field in magnetars

In order to describe magnetars, we make the following assumptions: (i) the dipole-like component dominates the field at long distances and matches the observed spin down within uncertainties. This constraint excludes purely toroidal magnetic fields. (ii) There are no currents in the magnetosphere, i.e. the exterior field is purely poloidal and is generated by the currents in the interior (type III). This assumption is justified by the estimate of Beloborodov (2009) that any twist in the magnetosphere should be dissipated on a timescale of ~ 1 year or shorter. Under this constraint a toroidal magnetic field can only exist in regions where magnetic field lines close inside the star (type I), and vanishes otherwise (type II). We note that some of the work on magnetars (Colaiuda et al. 2008; Lander et al. 2012; Colaiuda & Kokkotas 2011) use magnetic field configurations with a non-zero surface current to mimic unknown magnetospheric currents. We discuss below the relevance of these currents and their possible influence in our simulations. (iii) There are no current sheets or strong gradients in the magnetar interior because there is enough evolution time since the magnetar's birth to dissipate these. Therefore, we favour smooth functions with weak gradients across the star, i.e. we keep only low-order terms in the free functions of our magnetic field configurations.

According to these restrictions we consider three magnetic field regions in magnetars: (i) the region in the star, where magnetic field lines close in the interior, can be of type I, II or III, (ii) the region in the interior where magnetic field lines closing outside the star, can be of type II only (assuming that the currents generating the field originate in the interior of the star), and (iii) the exterior region of type III. It is convenient to treat all regions within the same framework using the current given by Eq. (21) for type I regions, and using the appropriate limits for $\tilde{H}_\varphi$ and $\mathcal{J}^i$ to construct the type II and III regions.

We computed the equilibrium models numerically using the LORENE library[2]. To do so we have modified the MAGSTAR tool of LORENE to account for the general form of the current (21) in Ampere's law (16). This new routine is called MAGNETSTAR. We neglect the magnetic field terms in the space-time and hydrostatic equilibrium equations, and use the same equations and numerical methods as in Bocquet et al. (1995). We first solve the equation for the unmagnetized equilibrium configuration, and then solve Ampere's law using the spherical spacetime and the density profile of the unmagnetized star as a background. We apply a fixed-point iteration to solve Ampere's law, starting with an initial current $\mathcal{J}^i_{\text{ini}}$. The resulting magnetic field configuration depends on the functions $M(A_\varphi)$ and $C_\varphi(A_\varphi)$, and on the initial current J^i_{ini} in the fixed-point iteration.

For $M(A_\varphi)$ we use the form

$$M(A_\varphi) = M_{\text{max}} \times \Big[a_0 \tilde{A}_\varphi + a_1 \tilde{A}_\varphi^2 + a_2 \tilde{A}_\varphi^3 $$
$$+ a_c \log\left(1 + \frac{\tilde{A}_\varphi}{c}\right) + d \Theta(A_\varphi - A_\varphi(x)) \Big] \tag{27}$$

where $\tilde{A}_\varphi \equiv A_\varphi/A_\varphi^{\text{max}}$, A_φ^{max} is the maximum of $|A_\varphi|$ inside the star, $A_\varphi(x)$ the value of A_φ at the equator at a distance x from the center, Θ the Heaviside step function, and a_0, a_1, a_2, a_c, and d are constant coefficients, which control the amplitude of the perturbation M, and c a parameter to control the shape of the current. The field strength of the respective configuration is controlled by M_{max}. Note that the expression following d leads to a delta function in the current, and corresponds to a infinitively thin circular current loop (Jackson 1998). For this case there exists an analytic solution which we use to avoid dealing with delta functions numerically.

For $\tilde{H}_\varphi(A_\varphi)$ we use the form

$$\tilde{H}_\varphi(A_\varphi) = b_0 \hat{A}_\varphi + b_1 \hat{A}_\varphi^2 + b_2 \hat{A}_\varphi^3, \tag{28}$$

where $\hat{A}_\varphi = (A_\varphi - A_\varphi^{\text{surf.max.}})/A_\varphi^{\text{max.}}$ with $A_\varphi^{\text{surf.max.}}$ being the maximum value of A_φ at the surface. The resulting B_φ is zero at the surface, and thus it is confined inside the star. The case $n = 1$ corresponds to one of the configurations in Lander & Jones (2012).

Regarding the initial current J^φ_{ini} we consider three configurations

spherical: $\mathcal{J}^\varphi_{\text{ini}} = \rho h j_0$,
dipole-like: $\mathcal{J}^\varphi_{\text{ini}} = \rho h j_0 r \sin\theta$,
quadrupole-like: $\mathcal{J}^\varphi_{\text{ini}} = \rho h j_0 r^2 \sin\theta\cos\theta$,

where j_0 is a constant parameter of the same order of magnitude as the coefficients used for the current (a_0, a_1 ...). The resulting magnetic field does not depend on the value of j_0 itself, and its strength is determined by the coefficients of Eqs. (27) and (28), i.e. a_i, b_i, a_c, and d, respectively.

Both the spherical and the dipole-like initial currents have

---

[2] http://www.lorene.obspm.fr

even symmetry with respect to the equator. This also holds when they are rescaled to the physically relevant $J_{(\varphi)} = \sqrt{\mathcal{J}_\varphi \mathcal{J}^\varphi}$. This $J_{(\varphi)}$ has a maximum at the equator and resembles a current loop. The corresponding magnetic field configurations are similar to that of a simple current loop (compare with the models in Sec. 3.1.4). Since the current loop is an idealization giving rise to a pure dipole field in the far field, we characterize the magnetic field configurations generated by the spherical or dipole-like currents as dipole-like. We note that in the near field regime, where the currents have finite spatial extension, other multipoles are always present. Both the spherical and the dipole-like initial current lead to the same final equilibrium configurations. Similarly, we call the magnetic field of a quadrupole-like initial current, which has odd symmetry with respect to the equator, a quadrupole-like magnetic field. In this case the dipole moment vanishes and the far field is dominated by the quadrupole component. To obtain these quadrupole-like configurations one must use those currents that are an odd function of A_φ. Otherwise the fixed-point iteration converges to the same dipole-like magnetic field as in the previous case. We denote by D and Q the configurations where the converged magnetic field is predominantly dipole-like or quadrupole-like, respectively.

Note that for the magnetic field configurations with non-vanishing parameters a_0, a_1, and b_0 terms appear in the current that are linear or constant in A_φ. Therefore, solutions corresponding to different parameters a_0, a_1, and b_0, can be linearly superimposed in the current to obtain further solutions. Using this procedure it is possible to compute configurations with a mixed dipole-quadrupole-like magnetic field (see Section 4).

We computed most of our initial models using the LORENE library and the procedure described above. However, in some cases where analytical solutions are known, we use these directly: the magnetic field originating from a ring current at a prescribed radius (see Section 3.1.4), and force-free configurations confined to the crust according to Aguilera et al. (2008) (see Section 5).

3   DIPOLE-LIKE CONFIGURATIONS

In this section we study the effects of different dipole-like magnetic field configurations on the Alfvén spectrum of a magnetar. We consider either a purely poloidal component (Section 3.1) or a mixed poloidal-toroidal field whose poloidal component is dipolar-like (Section 3.2). Our analysis is mainly based on the application of the semi-analytic model to investigate the behaviour of purely toroidal oscillations. Using this model we compute the Alfvén frequencies of individual field lines. The spectrum of the star is determined by the set of the frequencies of all field lines and the corresponding overtones given as a function of position inside the star. The position can be described by the point χ at which a field line crosses the equatorial plane or by the polar angle θ along a given radius. We also employ some numerical simulations to evaluate the quality of our approach.

3.1   Purely poloidal fields (type II)

We first discuss magnetar configurations with a purely toroidal current (type II). We generate the initial models using the procedure described in Sections 2.2.1 and 2.2.2, and the LORENE library. We focus on type II magnetic fields, which are completely defined by Eq. (27). The corresponding model parameters are given in Table 1. We obtain the desired magnetic field strength by rescaling $M_{\max}$. In the first three models (A$_0$, A$_1$, and C$_c$) only one parameter in

Model	a_0	a_1	a_2	a_c	c	Radius of ring in km
A$_0$	1	0	0	0	-	-
C$_c$	0	0	0	1	c	-
A$_1$	0	1	0	0	-	-
O	0	0.43	0.57	0	-	-
F	0.79	0	0.21	0	-	-
R$_\varpi$	-	-	-	-	-	ϖ

Table 1. Values of the current parameters of the employed models according to Eq. (27). The models R$_\varpi$ represent ring currents, ϖ denoting the radius of the ring in km.

Eq. (27) is different from zero (a_0, a_1, or a_c respectively). Additionally, we consider two different combinations of these parameters which are physically motivated. One of these, model F, results in a very flat spectrum and is expected to produce long-lasting QPOs and large gaps between the spectra of adjacent overtones of the Alfvén oscillations. Another model, model O, is chosen such that its spectrum reproduces some of the observed frequency ratios of SGR 1900+14.

The currents $\mathcal{J}^\varphi$ and the magnetic field configurations of the different models are displayed in Fig. 1 in the top and bottom panels, respectively. The different currents lead to very similar magnetic field configurations, all having their maximum either at the center of the star or along the equator, and a minimum in the center of the closed field lines. While the magnetic field lines look qualitatively very similar in all cases, the current distribution can be quite different.

Model A$_0$ has a spherically symmetric current distribution. The corresponding magnetic field is stronger along the polar axis than along the equator. It can be considered as the limiting configuration of model C$_c$ for $c \to \infty$. Varying the constant c, the spatial distribution of the current changes from being spherically symmetric, $c \gg 1$, to being aligned with the polar axis, $c \ll 1$ (see second and third panels in the top row of Fig. 1). The corresponding magnetic fields behave similarly, i.e. they align with the polar axis for $c \ll 1$ (bottom row).

By choosing a non-spherical current distribution, model A$_1$ (fourth column in Fig. 1), the maximum current is found at the equator near the outermost closed magnetic field line ($x \sim 6$ km). For this particular configuration the current vanishes at the polar axis. The resulting magnetic field is strongest in a central region oriented near the equator. Model O (fifth column in Fig. 1) looks very similar, but the current is somewhat more concentrated towards the equator, which leads to a weaker magnetic field close to the polar axis. Finally, model F has a flat spectrum (see below) and is characterized by two current maxima, one at the center and the other one at the equator at $x \sim 6$ km.

Due to their similar field configurations, the spectra of the corresponding Alfvén oscillations are quite similar (see Fig. 2). Near the polar axis ($\chi = 0$ km) all spectra have a turning point (U1) that can be either a maximum (A$_0$, C$_c$) or a minimum (A$_1$, F, O). Here, χ is the radius where the magnetic field line crosses the equatorial plane. The presence of turning points in the spectra is of particular interest, since QPOs are expected at the corresponding frequencies (Levin 2007; Sotani et al. 2008; Cerdá-Durán et al. 2009; Gabler et al. 2011, 2012). The QPOs close to the polar axis are called *Upper QPOs*.
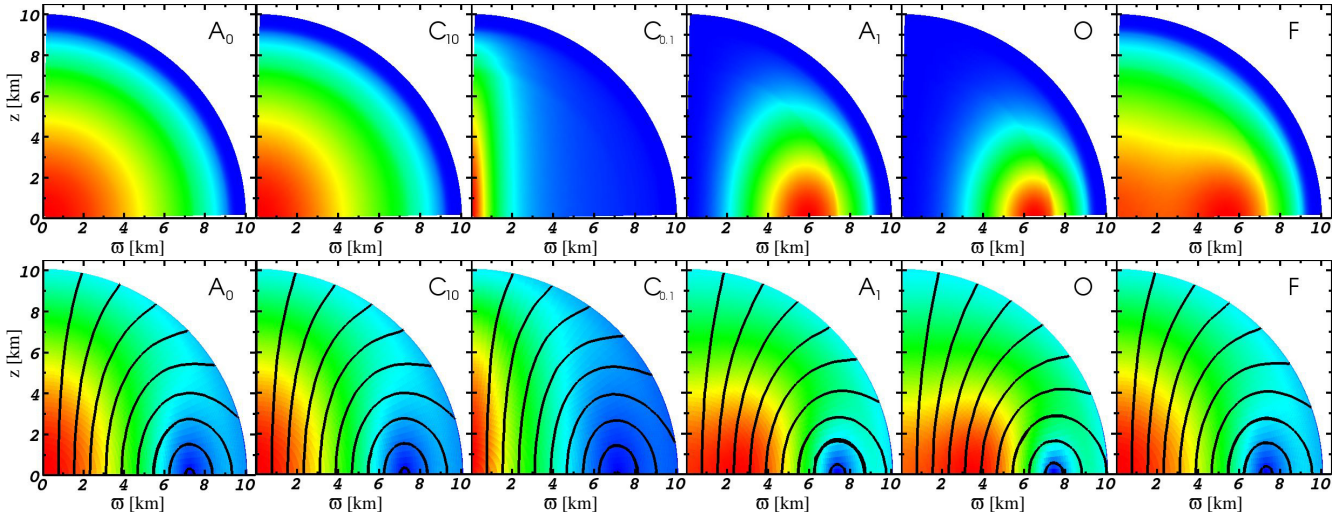
Figure 1. *Upper panels:* Current distribution $\mathcal{J}^{\varphi}$ for the model configurations (from left to right) A_0, C_{10}, $C_{0.1}$, A_1, O, and F . *Lower panels:* Corresponding magnetic field configurations with selected field lines. The colour scale ranges from blue (minimum) to red (maximum) and represents the current strength (top panels) and the strength of the poloidal magnetic field (bottom panels), respectively. Here and henceforth we use cylindrical coordinates z and ϖ to indicate the height and radial distance from the z-axis, respectively.

3.1.1 Single Upper turning point (U1)

Model A_0, black line in Fig. 2, was studied extensively in Gabler et al. (2011, 2012) and has a second turning point at the closed field lines at $\chi \sim 6.5$ km, which causes the appearance of the *Lower QPOs* (Cerdá-Durán et al. 2009). The spectra of the two models $C_{0.1}$ and C_{10}, magenta and light blue lines in Fig. 2, are qualitatively similar. The main difference between these two models is the gradient of the spectrum, which is stronger for the smaller value of c, because of the difference in rates at which the magnetic field strength decreases with increasing χ. For models where the electric current is concentrated more along the polar axis, the magnetic field close to the axis is stronger than for spherically symmetric currents, and it decreases faster with increasing χ. The stronger the magnetic field is close to the polar axis, the faster is the Alfvén speed in this region, i.e. the frequencies near the polar axis increase, too. (cf. model $C_{0.1}$). An abrupt change of the frequencies of the oscillations along neighbouring field lines is expected to lead to faster phase-mixing, which contributes to shorter lived QPOs (Levin 2007). Observing differences in the lifetimes of QPOs could in principle allow one to draw conclusions about the structure of the magnetic field close to the polar axis. Unfortunately, due to the numerical dissipation of our code we are not able to provide reliable estimates for the differences of the QPO lifetime caused by the different behaviour of the spectrum close to the polar axis.

The spectra for models C_c have a minimum in the closed field line region ($\chi \gtrsim 5$ km) only for $c \gtrsim 1$. Therefore, configurations with $c \lesssim 1$ do not have lower QPOs as observed in Gabler et al. (2012). However, this may not have strong observational consequences, because closed field lines couple only indirectly through the crust to the magnetosphere, i.e. we do not expect a strong modulation of the emission occurring in the magnetosphere at the frequencies of the possible lower QPOs.

The spectra of models A_1 and O are qualitatively different (red and blue line in Fig. 2). The turning point at the polar axis is a minimum for both models, and there exists a second turning point at $\chi \sim 5$ km, i.e. we expect a new family of QPOs (U2) besides the previously observed Upper (U), Lower (L) and Edge (E) QPOs.
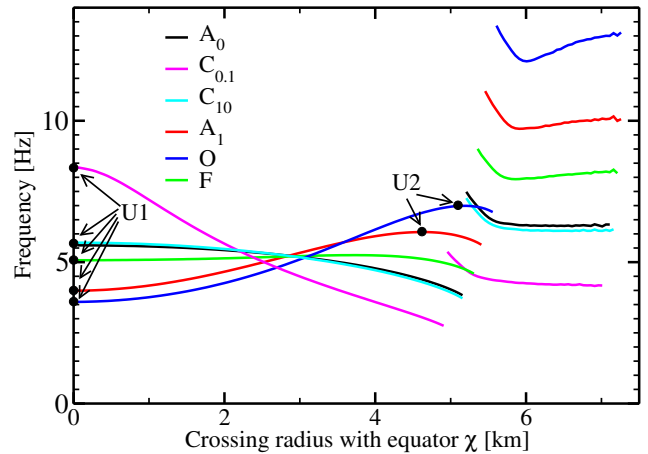
Figure 2. Alfvén spectra of the different magnetic field configurations given in Table 1. The spectra are obtained with our semi-analytic model at a surface-averaged magnetic field strength of 10^{15} G. The spectra for $\chi \lesssim 5$ km correspond to open field lines, while those for $\chi \gtrsim 5$ km to closed ones. Upper turning points (U1 and U2) are indicated black dots. The x-axis gives the point χ where the field line crosses the equatorial plane.

Edge QPOs are shorter-lived than turning-point QPOs. They are related to the edge of the spectrum at $\chi \gtrsim 5$ km, where the outermost open field line crosses the equator (see Gabler et al. 2012, for details).

Sotani et al. (2008); Cerdá-Durán et al. (2009) and Gabler et al. (2012) interpreted the observed QPO frequencies of 30, 92, and 150 Hz in SGR 1806-20 as the fundamental, the second and the fourth Alfvén overtones of the Upper QPOs, respectively. Similar arguments hold for SGR 1900+14 and the observed frequencies of 28, 84, and 155Hz. The surface-averaged magnetic field strength that matches the fundamental frequencies of both SGRs for the chosen current configurations is listed in Table 2. It shows that for models where the current has a maximum close to the polar axis ($C_{0.1}$, C_{10}, and A_0), the surface magnetic field strength neces-

Model	turning point polar axis (U1)		second turning point (U2)	
	B_{15} $f_0 = 28\,\mathrm{Hz}$	B_{15} $f_0 = 30\,\mathrm{Hz}$	B_{15} $f_0 = 28\,\mathrm{Hz}$	B_{15} $f_0 = 30\,\mathrm{Hz}$
A_0	4.9	5.3		
$C_{0.1}$	3.4	3.6		
C_{10}	4.9	5.3		
A_1	6.8	7.4	4.7	5.0
O	7.8	8.3	4.1	4.3
F	5.5	5.9		
R_4	4.1	4.4	3.4	3.6
R_5	5.4	5.9	3.0	3.2
R_6	7.4	7.9		
R_7	10.3	11.0		
R_8	14.3	15.2		

Table 2. Surface-averaged magnetic field strength needed to match a turning point of the spectrum to $f_0 = 28\,\mathrm{Hz}$ and $f_0 = 30\,\mathrm{Hz}$, respectively. The second and third column match the frequency of the turning point at the polar axis (U1), while the last two columns match the frequency of the second turning point (U2) in the spectrum, if present (A_1, O, R_4, and R_5).

sary to match the observed 30 Hz in the SGR 1806-20 giant flare is lower than for the other models (F, A_1, and O).

3.1.2 Two Upper turning points (U1 and U2)

The presence of the second turning point in models A_1 and O allows for an other interpretation of the observed QPOs of SGR 1900+14: One could identify the fundamental QPO ($U1_0$) and its second overtone ($U1_2$) with the observed frequencies of 28 Hz and 84 Hz, whereas the observed frequencies of 53 Hz and 155 Hz could correspond to the fundamental QPO at the second turning point ($U2_0$) and its second overtone ($U2_2$) (located at $\chi \sim 5\,\mathrm{km}$)[3]. Model O was constructed such as to fulfil this relation between the observed frequencies. The corresponding model parameters (Table 1) are not very peculiar, i.e. given the current theoretical uncertainties model O is as valid as any other model we could have constructed.

3.1.3 Nearly flat spectra: no shear modes inside continuum gaps

We choose the parameters of model F to obtain a very flat spectrum which is expected to produce very long-lasting QPOs in a large volume of the star. This happens because for almost all open field lines the QPOs have a very similar frequency. Additionally, the gap between successive overtones in the spectrum is maximized, which may allow for crustal shear modes surviving in these gaps (Colaiuda & Kokkotas 2011; van Hoven & Levin 2012) instead of being absorbed into the Alfvén continuum of the core as in Gabler et al. (2012). Hence, we have computed the spectra of the fundamental Alfvén oscillation and its first three overtones at $B_{15} = 3.7$. These spectra are shown in Fig. 3 together with the frequencies of the crustal shear modes (horizontal red dashed lines). The $l = 2$ and $l = 5$ shear modes with 24.8 Hz and 65.7 Hz, respectively, clearly fall between the frequencies of Alfvén overtones, while the frequencies for the $l = 3$ and $l = 4$ modes lie just on top of the maximum or at the edge. To search for the crustal
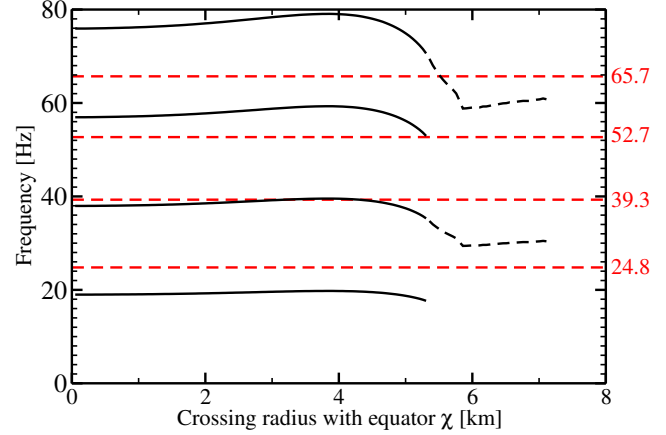
Figure 3. Alfvén spectrum of the magnetic field configuration F which leads to a very flat spectrum at $B_{15} = 3.7$. Red dashed lines indicate the frequencies of the crustal shear modes. The x-axis gives the point χ where the field line crosses the equatorial plane.
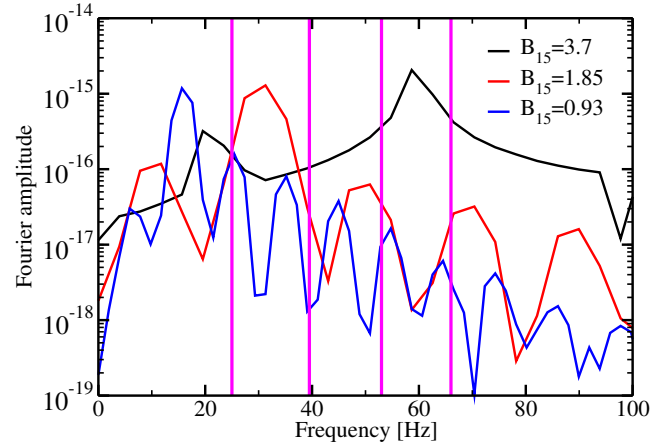

Figure 4. Fourier analysis of the oscillations at $B_{15} = 3.7$, 1.85, and 0.93. Magenta vertical lines indicate the frequencies of the first four crustal shear modes, whose precise values are given in Fig. 3.

shear modes which may have been survived, we performed simulations covering a period of 0.25 s, calculated the overlap integrals[4] with the pure crustal shear modes, and Fourier-analyzed them. The resulting Fourier transform for the $l = 2$ crustal shear mode at $B_{15} = 3.7$, 1.85, and 0.93 is given in Fig. 4. At $B_{15} = 3.7$ we find strong signals at the frequencies $f \sim 20$, 60, and 100 Hz. These are the frequencies expected from the semi-analytic model for the fundamental QPO and its second and fourth overtone (see Fig. 3). The frequencies of the overtones obey integer relations and do not behave as those of crustal shear modes which are proportional to $f_l \sim \sqrt{(l-1)(l+2)} f_0$. *None of the frequencies of the first three shear modes indicated by the magenta vertical lines in Fig. 4 coincides with an observed frequency of a QPO at $B_{15} = 3.7$.* Fig. 4 also shows that all observed QPOs scale directly with the magnetic field: the frequencies at $B_{15} = 3.7$ are twice as large as the corresponding frequencies at $B_{15} = 1.85$ and are four times as large

---

[3] We use subscripts to indicate overtones of the fundamental QPO frequency.

[4] Overlap integrals are global measures of how strong a given shear mode is excited. For details we refer to Gabler et al. (2012).
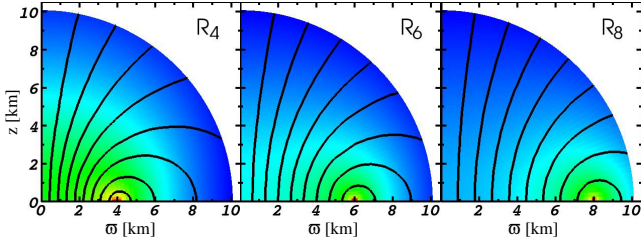
Figure 5. Magnetic field configuration for a ring current at a given radius as indicated in the panels. The colour scale ranges from blue (minimum) to red (maximum), and gives the logarithm of the magnetic field strength.
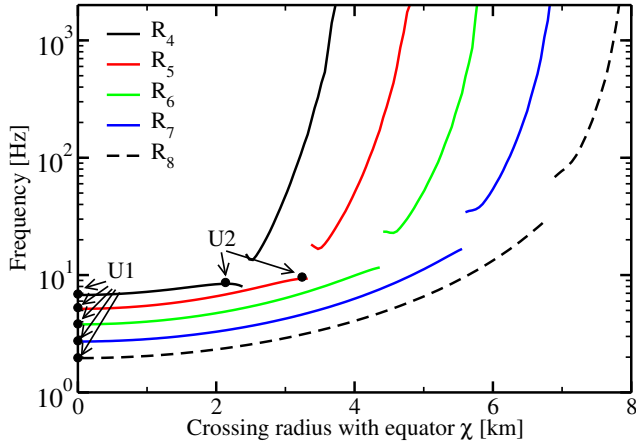
Figure 6. Alfvén spectra of magnetic field configurations obtained from ring currents R_ϖ at different radii ϖ. The spectra are calculated with our semi-analytic model for a surface-averaged magnetic field strength of $B_{15} = 1$. The x-axis gives the point χ where the field line crosses the equatorial plane.

as at $B_{15} = 0.93$. The matching of the frequency of the Alfvén overtone at $f \sim 25\,\mathrm{Hz}$ and at $B_{15} = 0.93$ with that of the $l = 2$ shear mode is pure coincidence.

Qualitatively the same result holds when analyzing the overlap integral for the $l = 3$ crustal shear mode. In this case all QPOs where the velocity field is symmetric with respect to the equatorial plane are discovered and, again, *no signal is present at the crustal shear modes*. The analysis with the overlap integrals is limited to oscillations having the same equatorial symmetry as the corresponding shear mode, i.e. the overlap integral is zero for the $l = 2$ ($l = 3$) mode and an oscillation of odd (even) symmetry with respect to the equatorial plane.

3.1.4 Ring current

Next we consider the extreme case of a magnetic field generated by a circular current loop inside the star, whose analytical Newtonian solution can be found in Jackson (1998). A ring current can be seen as a limiting case of model A_1 where the region of the current is shrunk to a ring. Placing the current at different radii we can construct different magnetic field configurations inside the neutron star (Fig. 5). The effects on the Alfvén oscillations are illustrated in Fig. 6, which displays the spectra for models R_ϖ where the ring currents are located at $\varpi = 4, 5, 6, 7,$ and $8\,\mathrm{km}$ from the center. In all cases the spectra have a minimum at the polar axis $\chi = 0\,\mathrm{km}$

Model	b_0	magnetic field strength [10^{12} G]		
		surface-averaged	max. poloidal	max. toroidal
B_0	0	3.5	19	0
B_1	1	3.6	20	3.5
B_2	2	4.0	21	7.1
B_5	5	5.6	24	18
B_{10}	10	7.6	27	33
B_{20}	20	8.9	31	54

Table 3. Surface-averaged, maximum poloidal and toroidal magnetic field strength for mixed poloidal-toroidal configurations with parameters $a_0 = 1$ and b_0 as indicated.
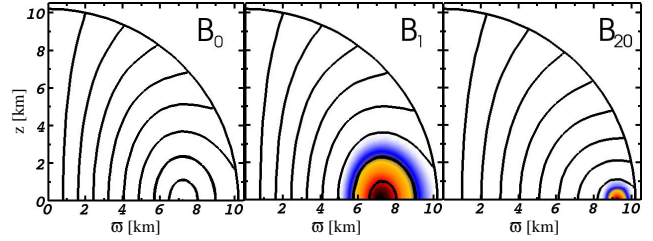
Figure 7. Magnetic field lines of different mixed poloidal-toroidal models. The colour scale gives the strength of the toroidal magnetic field and ranges from white-blue (minimum) to red-black (maximum). The field of model B_0 is purely poloidal.

(U1), and the frequency of the open field lines increases with increasing χ. Similar to model A_1 there is a second maximum at $\chi \sim 2.0\,\mathrm{km}$ and $\chi \sim 3.0\,\mathrm{km}$ for models R_4 and R_5, respectively. This second turning point may give rise to a new family of QPOs (U2) as discussed for models A_1 and O in the previous subsection.

The spectra associated with the closed field lines (right part of Fig. 6) show a strongly increasing frequency with increasing χ until the location of the ring current is reached. There are additional turning points for models R_4, R_5, and R_6 at $\chi \sim 2.5\,\mathrm{km}$, $\chi \sim 3.5\,\mathrm{km}$ and $\chi \sim 4.5\,\mathrm{km}$, respectively. However, the steepness of the spectra limits the existence of long-lived lower QPOs for these models, and for models R_7, and R_8 we do not expect lower QPOs at all.

3.2 Mixed poloidal-toroidal field (type I)

We turn now to models that have a mixed poloidal-toroidal field. In this case, the system of equations presented in Sec. 2.1 is no longer valid, as the toroidal component will couple axial and polar oscillations. However, since the toroidal component of our models is limited to the region of closed field lines inside the star, axial and polar oscillations still decouple at the linear level in the region of the open field lines. The coupling in the closed field line region will excite polar oscillations in the whole star. Fortunately, these do not influence the continuum at the linear level and we can still use our semi-analytic model to estimate the frequencies of the Alfvén oscillation in the region of open field lines.

Our models are obtained setting $a_0 = 1$ in Eq. (27) and Eq. (28) with different values for b_0. The surface-averaged magnetic field strengths and the maximum poloidal and toroidal field strength for the respective configurations are given in Table 3. The two components have similar strength at $b_0 \sim 10$. The field lines and the toroidal magnetic field strength of selected models are plotted in Fig. 7, which shows that the area occupied by the closed field
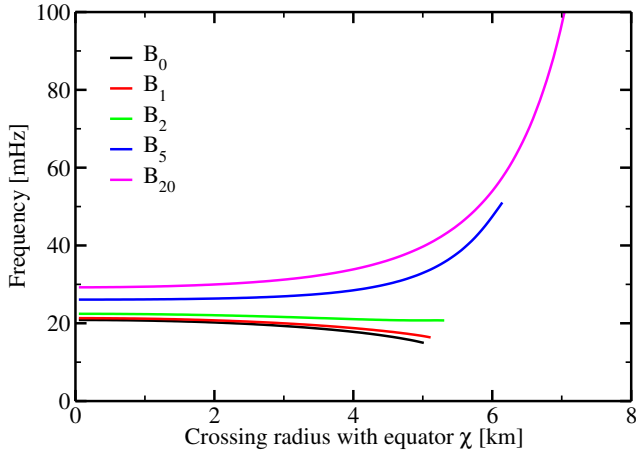
Figure 8. Alfvén spectra of torsional oscillations along the open field lines for mixed poloidal-toroidal models B_x obtained with our semi-analytic method. See Table 3 for model details. The x-axis gives the point χ where the field line crosses the equatorial plane.

Figure 9. Field lines of different mixed dipole-quadrupole-like (D-Q) configurations, the left panel showing the purely quadrupole-like case. The title of each panel indicates the Q-to-D component ratio. The red, dashed lines indicate the path along which the spectra of Fig. 10 have been obtained.
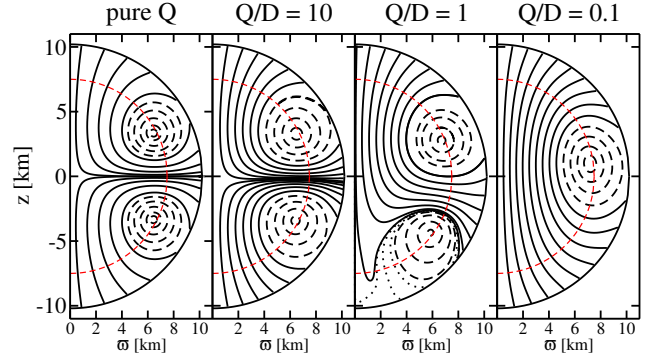
lines is largest in the case of zero toroidal field (model B_0). With increasing toroidal field this region shrinks and shifts towards the surface, see e.g. Lander et al. (2012). Additionally, the strength of the poloidal component increases at the closed field lines and at an limited region of the open field lines around the closed ones.

In Fig. 8 we plot the spectra of the open field lines of our mixed field models. For zero toroidal field the Alfvén spectrum is similar to the black line in Fig. 2, but scaled at different frequencies. There is a maximum at the polar axis ($\chi = 0$ km) and an edge at $\chi \sim 5$ km. With increasing values of b_0 not only the toroidal field increases but also the poloidal one. This increase is stronger near the closed field lines, such that the frequencies at large χ (~ 5 km) increase faster than closer to the polar axis, leading to a flatter spectrum in the case of model B_2 (green line in the figure). With an even stronger toroidal component, the turning point at the polar axis changes from a maximum to a minimum, and the Alfvén oscillations near the closed field lines ($\chi \sim 6$ and 7 km for models B_5 and B_{20}, respectively) show the highest frequencies. The larger b_0 is, the steeper the gradient of the spectrum becomes at the edge. In this case possible QPOs at the edge would last for shorter timescales than for model B_0 where the gradient of the spectrum is moderate.

4 MIXED DIPOLE-QUADRUPOLE-LIKE POLOIDAL CONFIGURATIONS

To obtain configurations with a quadrupole-like contribution we only consider for simplicity purely poloidal magnetic fields, i.e. type II magnetic fields, by setting $\tilde{H}(A_\varphi)$ equal to zero. Concerning the choice of parameters for the function $M(A_\varphi)$, only configurations that allow for a change of sign of $\mathcal{J}^\varphi$ across the equator and the corresponding initial data can be considered. In this section we choose $a_1 \neq 0$, while all other parameters are set to zero.

As we have mentioned in Section 2.2.2 we construct mixed dipole-quadrupole-like magnetic field configurations by linearly superimposing both currents, which are obtained independently. For the purely quadrupole-like (dipole-like) configuration, Q (D), $a_1 = 18.1$ ($a_0 = 11.66$) and the averaged surface magnetic field strength is $B = 6.0 \times 10^{13}$ G ($B = 4.4 \times 10^{13}$ G). When construct-

ing the mixed configurations we keep the dipole-like field strength fixed and add a quadrupole-like component rescaled by Q/D times the reference field.

The field lines of selected mixed configurations are displayed in Fig. 9. The configuration with $Q/D = 10$ is predominantly quadrupole-like, while $Q/D = 0.1$ gives rise to a slightly deformed dipole-like configuration. When the amplitudes of both components ($Q/D = 1$) are comparable, the field is very distorted, and has no symmetry with respect to the equatorial plane.

We emphasize that we study the mixed dipole-quadrupole-like configurations *without including a shear modulus in the crust*, in order to isolate the effect that the inclusion of a quadrupole-like component has on the continuum of torsional oscillations.

4.1 Alfvén spectra using the semi-analytic model

In Fig. 10 we plot the spectra of different combinations of Q and D. The x-axis gives the polar angle θ at which the field line crosses a circle with radius 7.5 km indicated with red, dashed lines in Fig. 9. This choice is motivated by capturing all field lines of the spectrum in one single parameterization . Fortunately, the center of the region(s) of closed field lines lies almost on this circle for all configurations studied here.

For $Q/D = 0.1$ (black lines in Fig. 10) the spectrum looks similar to the pure dipole-like case A_0. Qualitatively, we can identify the end of the line at $\chi \sim 5.2$ km in Fig. 2 with $\theta \sim 1.0$ rad in Fig. 10. Similarly, the local maximum at $\chi \sim 7.0$ km in one figure can be identified with the local maximum $\theta \sim 1.5$ rad in the other figure. We note the asymmetry between the two hemispheres ($\theta < \pi/2$ and $\theta > \pi/2$) due to the presence of the quadrupole-like component. There is a maximum at the polar axis in the northern and the southern hemispheres for the open field lines (solid lines in the figure) and a minimum inside the region of closed field lines (dashed lines in the figure) at $\theta \sim 1.1$. The latter field lines also form the minimum at $\theta \sim 1.7$. Additionally, there is another maximum at $\theta \sim 1.5$ that is associated with the closed field line which collapses into one point. Since this line has vanishing length, we do not expect to see a QPO at this location.

When the quadrupole-like component is half as strong as the dipole-like one, model $Q/D = 0.5$ (green lines in Fig. 10), there appear two new extrema in the spectrum of the open field lines at $\theta \sim 0.4$ (U2) and $\theta \sim 0.8$ (U3),respectively, which could produce QPOs. Additionally, the spectrum becomes fairly asymmetric
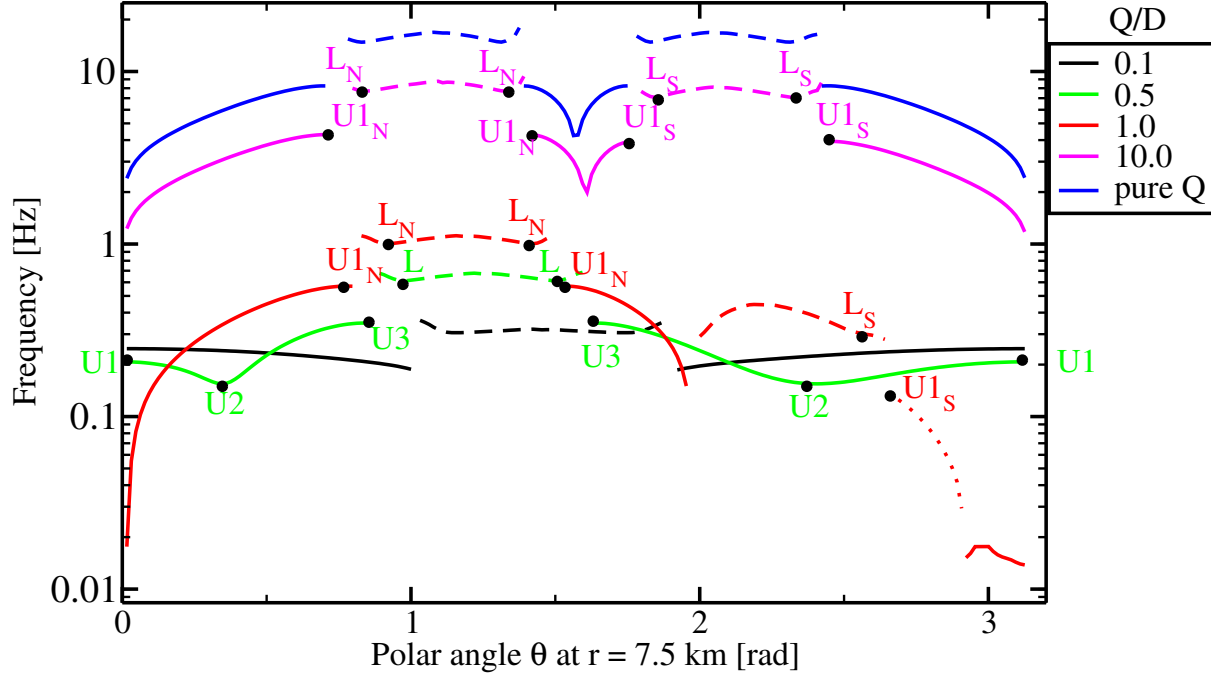
Figure 10. Alfvén spectra of different mixed configurations. Different line styles indicate regions of different types of field lines corresponding to Fig. 9. Solid lines correspond to open field lines, dashed lines to closed ones and the dotted line corresponds to open field lines only existing in the southern hemisphere for $Q/D = 1.0$. Selected turning points are indicated with black dots and labelled with U for Upper QPOs and L for Lower QPOs, respectively. The subscripts N and S stand for the hemisphere where the QPO appears, the northern $0 < \theta < \pi/2$ (N) and the southern $\pi/2 < \theta < \pi$ (S). The field strength of the dipole-like component is 4.4×10^{13} G, and the quadrupole-like component varies from 0.6×10^{13} G at $Q/D = 0.1$ to 6.0×10^{14} G at $Q/D = 10.0$, respectively. The pure quadrupole-like configuration is shown for $B = 1.2 \times 10^{15}$ G.

and the part due to the closed field lines (dashed lines in the figure) lies almost completely in the northern hemisphere $\theta < \pi/2$. At equal amplitudes of both magnetic fields, model $Q/D = 1.0$ (red lines in Fig. 10), the part of the spectrum due to the open field lines simplifies: the turning points at $\theta = 0.0$ and $\theta \sim 0.5$ disappear, and only the one maximum at $\theta \sim 0.75$ (U1$_N$) remains. The closed field lines part of the spectrum (dashed lines) in the northern hemisphere is now limited to the interval $0.8 \lesssim \theta \lesssim 1.5$., and for $2.0 \lesssim \theta \lesssim 2.5$ there appears a new family of closed field lines disconnected from the previous ones at smaller θ. The new closed lines have lower fundamental Alfvén frequencies, because the magnetic field in this area of the quadrupole-like component cancels partly with that of the dipole-like component, i.e. the resulting field is weaker than in the northern hemisphere. Additionally, there is a new family of open field lines (dotted red line in the figure) surrounding the closed lines at $\theta > \pi/2$, which we only observe for this particular combination $Q/D = 1.0$. They do not have any turning point, i.e. we expect at most very weak QPOs at the edges of the spectrum.

For increasing values of Q/D the frequencies increase for field lines with $\theta > 0.5$, because of the high magnetic field strength of the quadrupole-like component in this region. For the model with $Q/D = 10.0$ (magenta lines in Fig. 10) the symmetric spectrum of a pure quadrupole-like configuration is approached (see the blue lines in Fig. 10). For $Q/D = 10.0$ there is one turning point for the open field lines at $\theta \sim 0.7$ (U1$_N$) that is formed by the same field lines leading to another turning point at $\theta \sim 1.4$. They are also related to the two turning points (U1$_S$) at $\theta \sim 1.7$ and $\theta \sim 2.4$, respectively, caused by the mirrored field lines in the opposite hemisphere. The form of the spectrum associated with the closed field

lines almost does not change in the northern hemisphere $\theta < \pi/2$ compared to $Q/D = 1.0$, while the one in the southern hemisphere becomes symmetric to the one in the northern hemisphere. With increasing Q/D ratio, also the absolute values of the frequencies increase.

4.2 Alfvén QPOs using simulations

For the study of the time evolution of the Alfvén oscillations of the mixed dipole-quadrupole-like configurations we use the GRMHD code described in Sec. 2.1. The Fourier transforms of the strongest QPOs during the simulations for the configurations $Q/D = 0.5$, 1.0, and 10.0 are shown in the top, middle, and bottom rows of Fig. 11, respectively. We find oscillations at the frequencies predicted by the spectrum obtained with the semi-analytic model. The particular frequencies and names of the QPOs displayed in Fig. 11 are indicated in the upper right of each panel. We selected those QPOs which are best suited for the visualization considering different effects. For example, the particular initial perturbation applied to the equilibrium model may have excited some QPOs more than others. Some QPOs may have similar frequencies, i.e. their signals may overlap in the corresponding Fourier transform, which has a finite resolution. As expected, the spatial structure of the QPOs shown in the figure follows the structure of the magnetic field lines. For the $Q/D = 0.5$ (top row) the maximum amplitude of the Fourier transform for the $U1_0$ QPO (first column) is located near the polar axis, for $U3_1$ (fourth column) it is at the open field lines nearest to the closed field lines, while for $U2_2$ and $U2_4$ (second and fifth columns) the maximum amplitudes are found in between these two regions. The oscillation of L_0 (third column) is limited
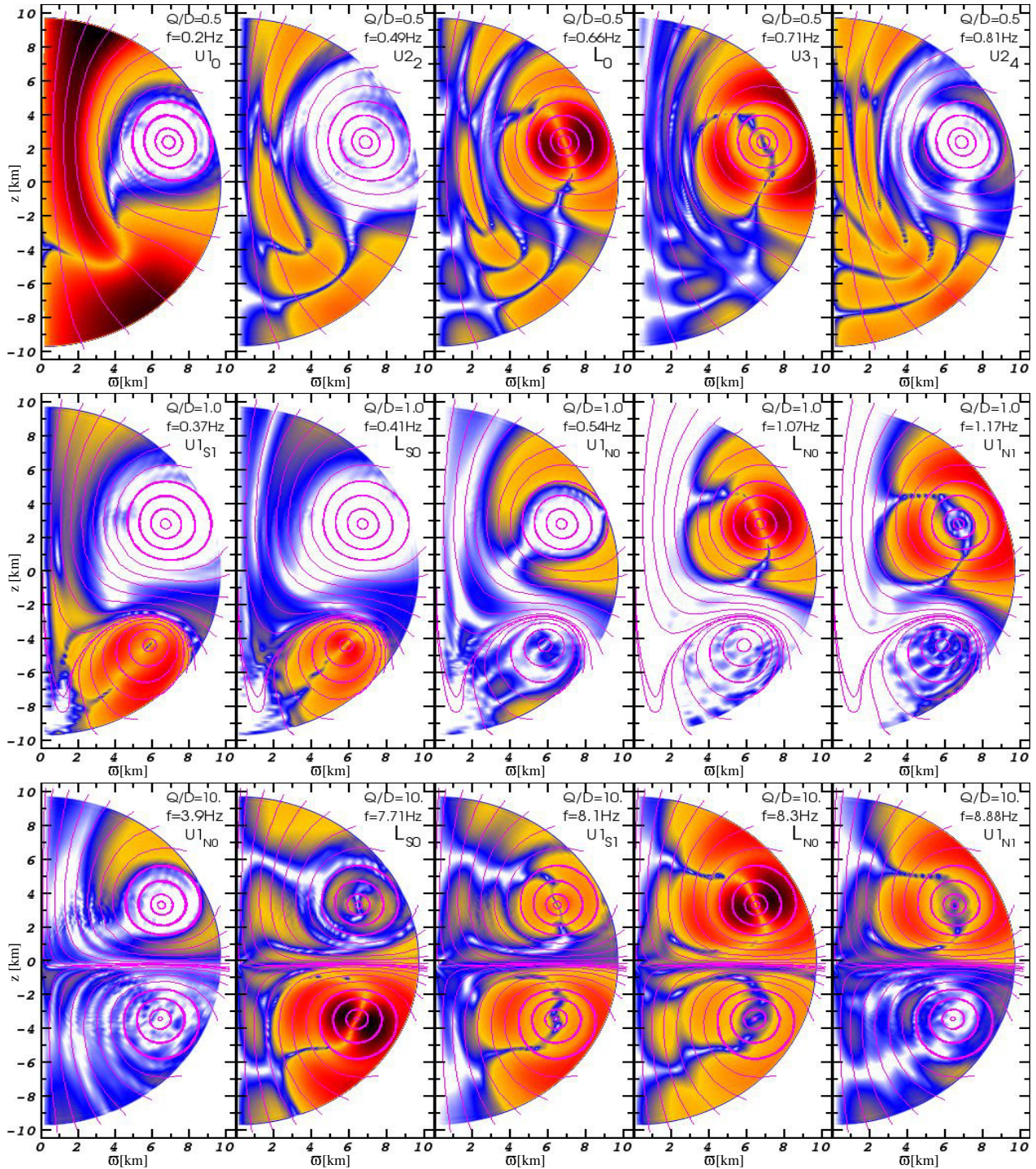
Figure 11. Fourier transforms of the Alfvén QPOs for configurations $Q/D = 0.5$ (top), $Q/D = 1$ (middle), and $Q/D = 10$ (bottom), respectively. The plotted QPOs are: $U1_0$, $U2_2$, L_0, $U3_1$, and $U2_4$ (top), $U1_{S1}$, L_{S0}, $U1_{N0}$, L_{N0}, and $U1_{N1}$ (middle) $U1_{N0}$, L_{S0}, $U1_{S1}$, L_{N0}, and $U1_{N1}$ (bottom). The subscript indicates the number of the overtone, with 0 indicating the fundamental QPO. In all panels the colour scale ranges from white-blue (minimum) to red-black (maximum) and gives the logarithm of the Fourier amplitude of the QPOs at the frequency denoted in the upper right of each panel.

to the closed field lines. In the third column we can also see three overtones of the different Upper QPOs: $U1_2$ (three nodes near the polar axis), $U2_3$ (four nodes), and $U3_1$ (two nodes along the open field lines close to the closed ones), which all have approximately the same frequency.

The QPOs of the configuration with $Q/D = 1.0$ are plotted

in the middle row of Fig. 11 and are labelled $U1_{S1}$, L_{S0}, $U1_{N0}$, L_{N0}, and $U1_{N1}$ (from left to right, respectively). The additional subscripts N and S indicate the northern or southern hemisphere where different QPOs are localized. $U1_{S0}$ and L_{S0} are the fundamental oscillations of the open and closed field lines in the southern

hemisphere, while $U1_{N0}$, L_{N0}, and $U1_{N1}$ are limited to the northern one.

For $Q/D = 10$ (bottom row) both hemispheres approach a similar magnetic field configuration, which results in an almost symmetric distribution of the oscillations. In most of the panels (2-4) of this row we see a strong Fourier amplitude in both hemispheres. This is expected because the frequencies of the corresponding QPOs in the northern and southern hemispheres are almost equal. However, there are still some small differences in the frequencies, e.g. between $U1_{S1}$ ($f \sim 8.1$ Hz) and $U1_{N1}$ ($f \sim 8.9$ Hz), or between L_{S0} ($f \sim 7.7$ Hz) and L_{N0} ($f \sim 8.3$ Hz), respectively.

5   MAGNETIC FIELD CONFIGURATIONS CONFINED TO THE CRUST

We now turn to the study of magnetic field configurations that are confined to the crustal region of the neutron star. In such cases the crustal shear modes cannot be absorbed by the core. Our choice is motivated by the possible presence of superconducting protons in the core of the neutron star (Page et al. 2011; Shternin et al. 2011) which could expel the magnetic flux due to the Meissner-Ochsenfeld effect. From theoretical studies (Baym et al. 1969) one would expect the protons to form a superconductor of type II, the magnetic field being able to penetrate the superconducting region in form of flux tubes. However, due to the uncertainty of the EoS at supranuclear densities, the opposite situation cannot be ruled out completely. In the present context we only consider the effects of type I superconductivity on the Alfvén spectrum of torsional modes. The only other existing study of such a configuration (but with an additional toroidal component and assuming a discrete spectrum of modes) was presented by Sotani et al. (2008).

We follow Aguilera et al. (2008) who give a description of different axisymmetric magnetic field configurations. We neglect the effects of general relativity on the magnetic field and the influence of the magnetic field on the neutron star structure. This should be a valid approach, in particular, for fields confined to the crust containing only a few per cent of the total stellar mass. Moreover, we assume that the magnetic field has relaxed to some equilibrium before the crust crystallized. After crystallization the magnetic field is frozen into the crust. For simplicity, we consider purely poloidal fields only. These models can be described by the type III magnetic field of Section 2.2.1. The corresponding currents outside the crust determining the magnetic field structure are the superconducting currents at the crust-core interface. Details on how to construct magnetic fields confined to the crust are given in Appendix A.

We study different configurations, namely magnetic fields matched to an exterior dipole, quadrupole, or octupole field. The amplitudes of the magnetic field at the surface of such configurations a have different angular dependence. To compare the results, we thus label the different configurations with their averaged magnetic field strength at the surface of the star, and use this value as reference magnetic field strength.

The field topology of the configurations and the corresponding spectra of the purely Alfvén oscillations at $B = 10^{14}$ G are given in Fig. 12. The parts of the Alfvén spectrum associated with a particular family of field lines share the same colour in the graphs showing the spectrum and the magnetic field configuration. If the magnetic field is confined to the crust the maximum field strength is found near the crust-core interface. The maximum strength for the dipole-like (quadrupole-like, octupole-like) configuration is about 13 (8,

8) times the average value at the surface. This is a factor of a few stronger than the crustal field of configurations penetrating the core. Consequently, the structure of the magnetic field varies on smaller scales. There are field lines which close inside the crust, e.g. near the equator for the dipole-like (red lines in Fig. 12) and octupole-like (green lines) configurations, or at $\theta \sim 60°$ for quadrupole-like and octupole-like configurations (see blue lines in Fig. 12). Because of stronger magnetic fields and stronger field gradients on smaller spatial scales, we need higher numerical grid resolution for our simulations (see below) and expect higher frequencies of the Alfvén oscillations.

In the following we will refer to magnetic field configurations matched to an exterior dipole as configuration D, to an exterior quadrupole as Q, and to an octupole as O, respectively.

5.1   Alfvén spectra with the semi-analytic model (without shear)

Let us first discuss the spectra obtained with the semi-analytic model of Cerdá-Durán et al. (2009) and Gabler et al. (2012) displayed in the lower panels of Fig. 12. First, we note that for configurations matched to an exterior quadrupole and octupole, there are no turning points present inside the continuum of the open field lines. Therefore, one would expect QPOs only at the edges of the different branches of the continua. For the dipole-like case we observe a turning point only at the very high frequencies at field lines located around the closed field lines at the equator (corresponding to the upper end of the red coloured part of the spectrum). Second, the frequencies of the fundamental oscillation of the short closed field lines ($> 100Hz$) are higher than the frequencies we observe for a magnetic field penetrating the core (a few Hz at 10^{14} G). The frequencies of the field lines near the polar axis are similar to those obtained for a magnetic field configuration penetrating the core. Note that there is a edge at $\theta = 0$, and that the corresponding frequencies are finite.

5.2   Alfvén QPOs from simulations (without shear)

The semi-analytic model shows that the spectra of magnetic fields confined to the crust are very steep near the edges and posses a turning point for configuration D at very high frequencies. Moreover, the field lines near the edges are packed very densely along the crust-core interface leading to enhanced phase mixing. Therefore, we expect more difficulties to observe QPOs with significant amplitudes in our numerical simulations. As mentioned before, the requirements on the grid resolution are more stringent, because of the finer spatial structure of the magnetic field. The grid resolution employed for the time evolution of the three magnetic field configurations (at $B = 10^{14}$ G) is 30×80 ($r \times \theta$) for $[r_{cc}, r_s] \times [0, \pi]$. All models have been evolved for up to 5 s.

Indeed, the Fourier analysis displayed in Fig. 13 shows less significant amplitudes of the QPOs than in the case of global magnetic field configurations penetrating the core. Nevertheless, we can identify some QPOs as local maxima of the Fourier amplitude. The QPOs for the dipole-like configuration (upper panels) have their maximum amplitudes near the polar axis. This is expected, because the edge of the continuum is located there. With the numerical resolution used we were not able to see the other edge of the continuum
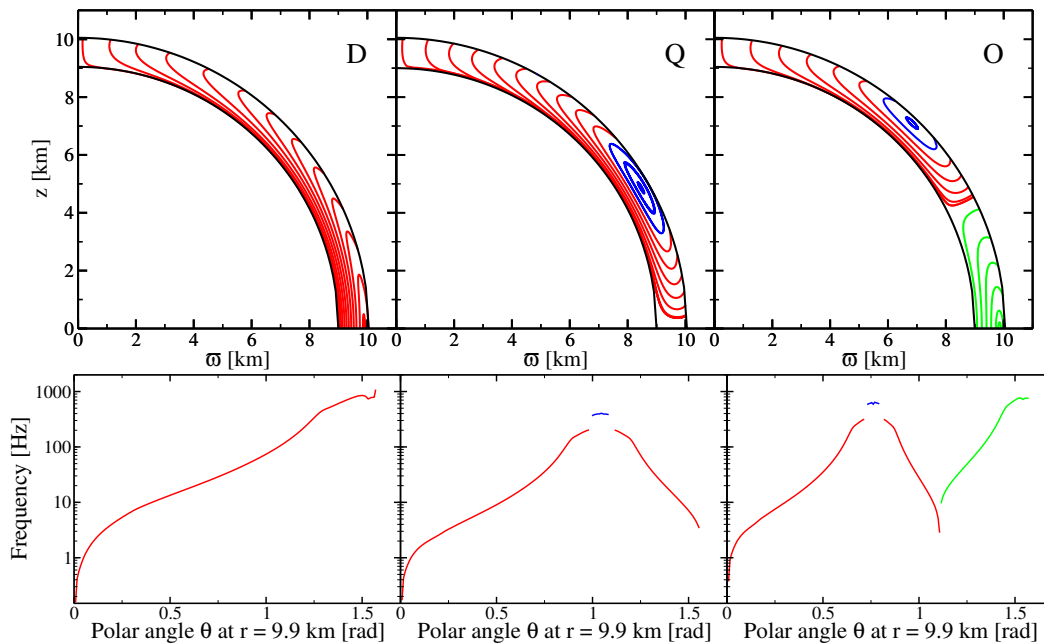
Figure 12. *Upper panels*: Magnetic field configurations for models matched to an exterior dipole (left), quadrupole (middle), and octupole (right), respectively. *Lower panels*: Alfvén spectra of the magnetic field configurations given in the corresponding upper panel obtained with the semi-analytic model for an averaged surface magnetic field of $B \sim 10^{14}$ G. Corresponding field lines in the upper and lower panels have the same colour.

at much higher frequencies, because the associated field lines near the equator have a very small spatial extension[5].

The quadrupole-like magnetic field has closed field lines near $\theta \sim 1.0$ rad (see Fig. 12). The corresponding frequencies of the continuum are > 100 Hz. Unfortunately, the affordable grid resolution is too low to analyze potential QPOs for these field lines. Therefore, we find QPOs only for the continuum of the open field lines. These are best seen in the plot for 4.3 Hz in the middle panel of Fig. 13. Only open field lines oscillate at the given frequency and have large Fourier amplitudes near the polar axis and equator. Closed field lines, on the other hand, do not participate in these oscillations, as the Fourier amplitude vanishes in the corresponding regions.

When the magnetic field is matched to an exterior octupole, we find oscillations of the open field lines (best visible for $f = 3.9$ Hz in the bottom panel of Fig. 13). The red-coloured field lines in the right panel of Fig. 12 do not extend to the equator, and the corresponding QPO has a large amplitude around $\theta \gtrsim 1.0$ rad. At 0.9 Hz we find oscillations with significant amplitudes also for the field lines near the equator. At almost all frequencies there is a non-vanishing Fourier amplitude at the closed field lines around $\theta \sim 0.75$ and $\theta = \pi/2$, which is probably caused by the too low grid resolution.

In none of the cases considered is it possible to clearly associate the observed QPOs with features of the semi-analytic spectrum obtained in Sec. 5.1, because the frequencies do not match

perfectly. Nevertheless, a conservative interpretation would be that some QPOs which are associated with the open field lines near the polar axis correspond to the edges of the continuum and their overtones. The closed field lines are expected to oscillate at frequencies above 100 Hz which we cannot confirm because of lack of spatial resolution. Furthermore, we are mainly interested in the frequency range below 100 Hz and models where the elastic properties of the crust are included (see Section 5.3). Additionally, as a consequence of the finer spatial structure of the magnetic field confined to the crust, there is a much stronger numerical coupling of different field lines, which leads to enhanced damping and weaker QPOs. We expect this weakness of our approach to be less important in the coupled scenario, because for sufficiently low magnetic fields, the oscillations will be dominated by the shear in the crust. The corresponding modes are sufficiently resolved at the numerical resolution applied here.

5.3 Coupled magneto-elastic oscillations

We now investigate the behaviour of coupled magneto-elastic oscillations of the crust for the magnetic field configurations considered above. Therefore, we performed a number of simulations with initial data consisting of a general perturbation with an angular dependence of the sum of the $l = 2$ and 3 vector spherical harmonics at different magnetic field strengths. In the following we will use the letter l' to label shear-mode-like QPOs inside the crust, where l' is the number of nodes in θ-direction. For non-vanishing magnetic fields, these QPOs are no longer normal mode oscillations, but QPOs with time-varying spatial structure. Therefore, they do not have the angular dependence of individual vector spherical harmonics and they cannot be described by simple analytic functions. The chosen grid resolution for the simulations depends on the selected model and on the radius at which the crust-core interface r_{cc} is located. The smallest resolution used consisted of 60×80

---

[5] To resolve these smaller scales, the grid resolution has to be refined significantly. However, we need to evolve the models for several dynamical time scales of the low frequency oscillations around 1 Hz, which takes the order of several days of computing time with the current resolution. Since we are mainly interested in the frequency range around 30 Hz, we had to find a compromise between the computational effort and the scanned frequency range.
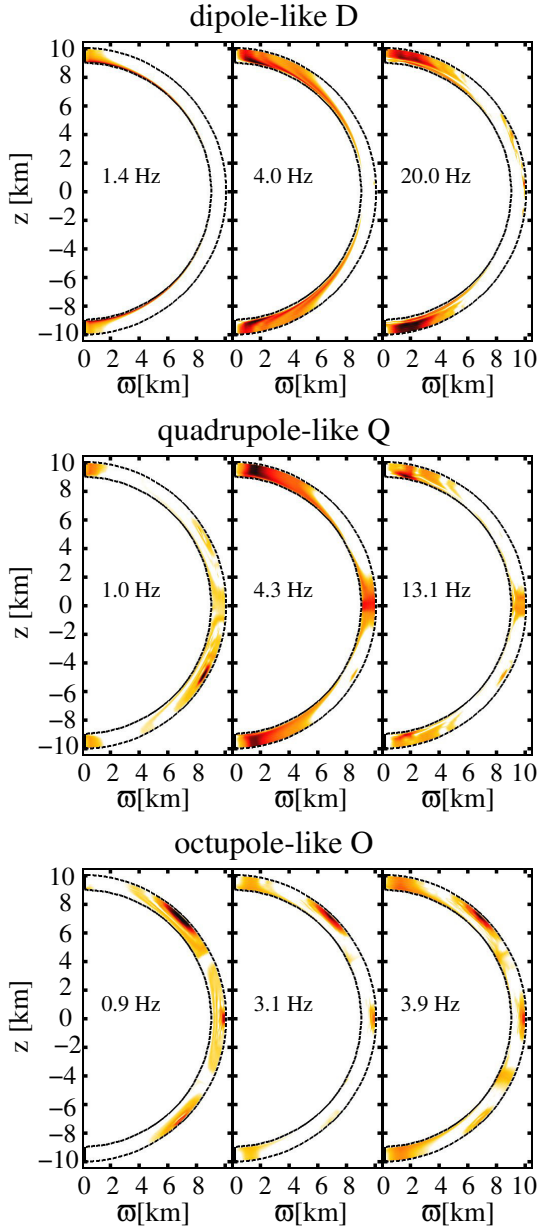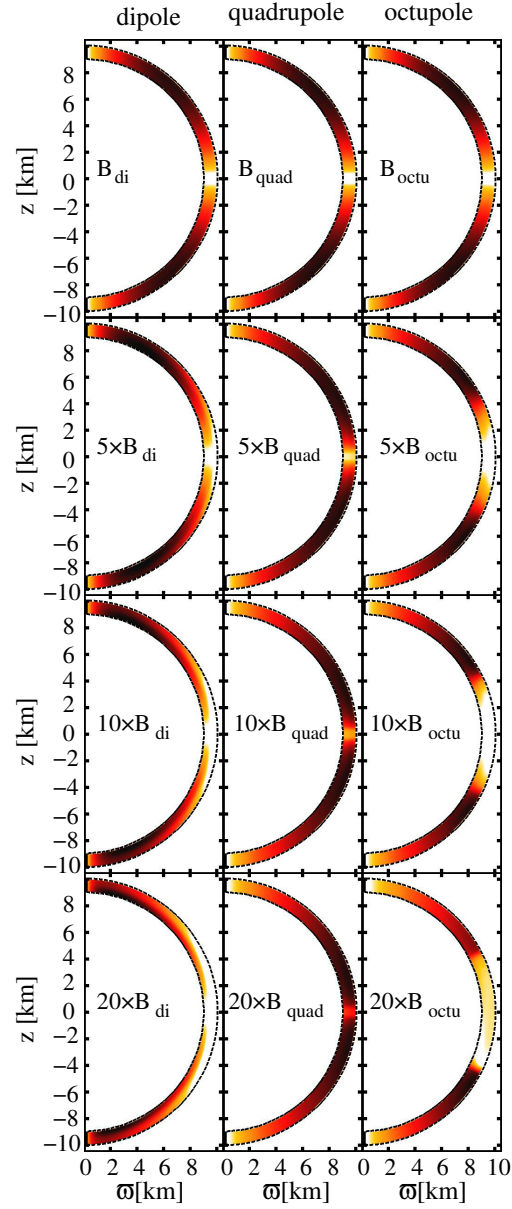
Figure 13. Spatial structure of the low-frequency QPOs obtained by a Fourier analysis of different magnetic field configurations. *Upper panels*: configuration D; *Middle panels:* configuration Q: *Lower panels:* configuration O. The corresponding frequencies are given, too. The colour scale ranges from white (minimum) via red to black (maximum).

Figure 14. Fourier amplitude of the $l' = 2$ crustal shear mode and its magneto-elastic generalization for different magnetic field configurations and different field strengths. The colour scale ranges from white (minimum) via red to black (maximum).$B_{di} = 1.7 \times 10^{14}$ G, $B_{quad} = 1.9 \times 10^{14}$ G, and $B_{octu} = 1.2 \times 10^{14}$ G, respectively.

$(r \times \theta)$ points for $[r_{cc}, r_s] \times [0, \pi]$. The integration time is $t \sim 2$ s at $B = 10^{14}$ G. For stronger fields, the integration time scales inversely with the magnetic field strength.

The results of the Fourier analysis of these simulations are plotted in Fig. 14, where we focus on the Fourier amplitude of the magneto-elastic generalization of the $l' = 2$ shear mode for different magnetic field strengths and different field configurations (dipole-like, quadrupole-like, and octupole-like). The averaged surface magnetic field strengths are $B_{di} = 1.7 \times 10^{14}$ G, $B_{quad} = 1.9 \times 10^{14}$ G, and $B_{octu} = 1.2 \times 10^{14}$ G, respectively. When making general statements holding for all three magnetic field configurations we use the label B_x.

At $B = B_x$ (first row of Fig. 14) the structure of the magneto-elastic QPOs is very similar to that of the purely crustal shear modes for all three field configurations, and for all shear modes. The corresponding panels in Fig. 14 show how the purely crustal shear modes approximately look like. For larger magnetic field strengths, the assumed magnetic field configuration changes the structure of the shear modes. For example, in the presence of a dipole-like surface field, the $l' = 2$ QPO is compressed towards those field lines entering the star closer to the pole. The stronger the magnetic field is the closer to the polar axis the QPO are located (see at the leftmost panels of the figure from top to bottom). This resembles the behaviour of the QPOs of purely Alfvén oscillations for this configuration (see Fig. 13). On the other hand,
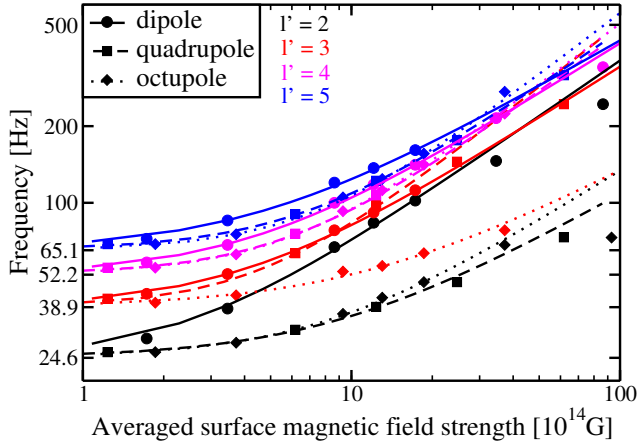
Figure 15. Dependence of the frequencies of the $n = 0, l' = \{2, 3, 4, 5\}$ QPOs on the magnetic field strength for different magnetic field configurations which are confined to the crust. The purely crustal shear mode frequencies are given at the y-axis label as 24.6, 38.9, 52.2, and 65.1 Hz, respectively. The lines are fits according to Eq. (30), and the corresponding parameters are given in Table 4.

l' (nodes along θ)	field	$B_{\rm crit}$ [10^{14} G]	$b_{l'}$
2	dipole-like	2.5	1.46
2	quadrupole-like	8.4	1.21
2	octupole-like	9.0	1.35
3	dipole-like	4.1	1.35
3	quadrupole-like	4.7	1.70
3	octupole-like	13.1	1.14
4	dipole-like	4.3	1.33
4	quadrupole-like	5.9	1.55
4	octupole-like	6.5	1.61
5	dipole-like	4.6	1.22
5	quadrupole-like	6.7	1.46
5	octupole-like	7.8	1.63

Table 4. Parameters $B_{\rm crit}$ and $b_{l'}$ of Eq. (30) for different magnetic field configurations and different number of nodes in θ-direction l'.

the QPO structure of quadrupole-like surface fields (central panels) behaves in the opposite way, i.e. the maximum amplitude is shifted towards the equator with increasing magnetic field strength. Finally, for an octupole-like configuration (rightmost panels), the maximum Fourier amplitude remains at approximately its original position but it becomes narrower with increasing magnetic field strength. For the corresponding change in the frequency of crustal shear modes with $l' > 2$ (not shown in the figure) we observe a similar behaviour depending on the particular field configuration: The stronger the magnetic field, the more the structure of the QPO tends to resemble the structure of that field, and the shear modes are expelled from regions of closed field lines (see e.g. the region close to the equator for configurations D and O in Fig. 13).

A common feature of all configurations is that with increasing magnetic field strength the identification of QPOs becomes more difficult because their amplitudes decrease. That is why some QPOs are not present at all field strengths. In particular, we have not succeeded in identifying the following QPOs: $l' = 4$ at $B = 10 \times B_{\rm quad}$ and $B = 20 \times B_{\rm quad}$, and $l' = 5$ at $B = 20 \times B_{\rm octu}$, respectively. For even stronger magnetic fields $B = 50 \times B_{\bf x}$ it is almost impossible to identify the magneto-elastic generalizations of the crustal shear modes, as the evolution is completely dominated by the magnetic field.

In order to understand how the frequencies of the shear modes change, when they become QPOs in the presence of the magnetic field we display in Fig. 15 the QPO frequencies as a function of the averaged surface magnetic field strength. Different colours indicate different QPOs associated with the zero-magnetic-field shear modes (black: $l' = 2$; red: $l' = 3$; magenta: $l' = 4$; blue: $l' = 5$). The line style indicates the magnetic field configuration (solid: dipole-like; dashed: quadrupole-like; dotted: octupole-like). At a surface magnetic field strength of about a few$\times 10^{14}$ G the frequencies of the QPOs begin to deviate significantly from those of purely shear modes. For the $l' = \{2, 3, 4, 5\}$ modes the zero-magnetic-field frequencies are 24.6, 38.9, 52.2, and 65.1 Hz, respectively, and are marked along the y-axis

Sotani et al. (2008) studied similar magnetic field configurations and found an increase of the frequency of the QPOs with in-

creasing magnetic field. Sotani et al. (2007) give an approximate formula of the dependence of the frequency on the magnetic field

$$\frac{f_{l'}(B)}{f_{l'}^0} = \sqrt{1 + a_{l'}\left(\frac{B}{B_\mu}\right)^2}, \qquad (29)$$

where $f_{l'}^0$ is the frequency of the purely shear eigenmode, and $B_\mu = 4 \times 10^{15}$ G. When fitting the frequencies obtained in our simulations with this formula we find a fairly inaccurate correspondence. Therefore, we generalized Eq. (29) to

$$\frac{f_{l'}(B)}{f_{l'}^0} = \sqrt{1 + \left(\frac{B}{B_{\rm crit}}\right)^{b_{l'}}}, \qquad (30)$$

where $B_{\rm crit}$, is the magnetic field strength at which the influence of the magnetic field becomes important. The parameters $B_{\rm crit}$ and $b_{l'}$ are given in Table 4, and the corresponding fits are displayed in Fig. 15. Note that we only used the values for $B \leqslant 10 \times B_{\bf x}$ for the fits because either we could not find shear-mode-like oscillations for stronger fields or their identification was difficult.

The observed exponents deviate significantly from $b_{l'} = 2$, the majority being $4/3 \lesssim b_{l'} \lesssim 5/3$. For very strong magnetic fields (about several$\times 10^{15}$ G, see Gabler et al. 2012) one would expect a transition to Alfvén oscillations, where the frequency depends linearly on B, i.e. $b_{l'} \to 2$. However, in the presence of such strong fields, shear oscillations no longer exist. In the regime studied here we expect a significant influence of the shear modulus such that the asymptotic regime of $b_{l'} = 2$ is not reached yet, which may explain the deviation from $b_{l'} = 2$.

While there is no clear dependence of the exponent $b_{l'}$ on the magnetic field configurations, one should note that the critical surface field $B_{\rm crit}$ is slightly lower for the dipole-like configuration than that for configurations Q and O for all QPOs and for all l'. This can be explained with the magnetic field structure. First, the configuration D has the strongest magnetic field inside the crust ($\sim 13 \times B_{\rm surf}$) for a given surface field compared to the other two ($\sim 8 \times B_{\rm surf}$). Second, the $n = 0$ shear modes[6] travel predominantly in θ-direction. Therefore, the θ-component of the magnetic field should be the dominant one to enhance the mode propagation velocity and, hence, to increase the frequency of the QPOs. In contrast to configuration Q and O, which both have more than one node

---

[6] n is the number of nodes in radial direction.

of the θ-component of the magnetic field in θ-direction, the dipole-like configuration has only one node at the polar axis. Thus, the averaged absolute value of the θ-component is stronger for configuration D and we expect it to influence the magneto-elastic waves more strongly than in case of the other two configurations.

We can extrapolate our results given by Eq. (30) to different values of the shear modulus and test whether a change of this parameter can explain the lowest observed frequencies of 18, 26, and 30 Hz in SGR 1806-20, as proposed by Steiner & Watts (2009). This approach should be a very good approximation for the $n = 0$ modes, because their frequencies are mainly determined by the shear modulus and depend only very weakly on additional constraints from the EoS, such as the thickness of the crust (Samuelsson & Andersson 2007).

If the shear modulus μ_s is divided by a factor F, the system of equations (5), (10), and (11) conserves its form if we rescale the background magnetic field B^k by the square root of this factor and simultaneously multiply the time by $\sqrt{F}$:

$$\frac{\partial \sqrt{\gamma} S_\varphi}{\partial \tilde{t}} = \frac{\partial \sqrt{-g}(b_\varphi \tilde{B}^k + 2\tilde{\mu}_s \tilde{\Sigma}^k_{\ \varphi})}{\partial x^k} , \tag{31}$$

$$\frac{\partial \sqrt{\gamma} B^\varphi}{\partial \tilde{t}} = \frac{\partial \sqrt{-g} v^\varphi \tilde{B}^k}{\partial x^k} , \tag{32}$$

$$2 g_{kk} g^{\varphi\varphi} \frac{\partial \tilde{\Sigma}^k_{\ \varphi}}{\partial \tilde{t}} = \frac{\partial \tilde{\xi}^\varphi_{,k}}{\partial \tilde{t}} = \frac{\partial v^\varphi \alpha}{\partial x^k} , \tag{33}$$

where $\tilde{t} = t\sqrt{F}, \tilde{\Sigma}^k_{\ \varphi} = \Sigma^k_{\ \varphi}\sqrt{F}, \tilde{B}^k = B^k/\sqrt{F}$, and $\tilde{\mu}_s = \mu_s/F$, respectively.

The rescaling of the time coordinate implies an inverse rescaling of the frequency. Therefore, we obtain the expected result that in the absence of a magnetic field the frequencies of the crustal shear modes scale as $1/\sqrt{F}$. A decrease of the shear modulus by a factor F leads to a corresponding decrease of the QPO frequency by $\sqrt{F}$. Consequently, the critical magnetic field for an equilibrium model with a rescaled shear modulus (divided by F) has to be divided by $\sqrt{F}$. Knowing $B_{\rm crit}$ and $b_{l'}$ for an equilibrium model we can compute the frequency of the QPOs for different shear moduli by

$$f_{l'}(B) = \frac{f^0_{l'}}{\sqrt{F}} \sqrt{1 + \left(\frac{B}{B_{\rm crit}/\sqrt{F}}\right)^{b_{l'}}} . \tag{34}$$

The corresponding curves for the dipole-like background configuration, the lowest QPO with $l' = 2$, and $F = \{2, 4, 8, 16, 100\}$ are given in Fig. 16. Clearly, the decrease of the shear modulus leads to a decrease of $B_{\rm crit}$, i.e. the magnetic field becomes dynamically dominate at lower magnetic field strength than for large μ_s. With the dipole-like configuration we are not able to find oscillations at frequencies of 18 , 26 or 30 Hz at any value of the shear modulus up to 1/16th of its tabulated value for $B \gtrsim 6 \times 10^{14}$ G, which is the lower bound for the dipole-like magnetic field of the magnetars showing giant flares from spin-down estimates. Only for the unrealistically small value of $\tilde{\mu}_s = \mu_s/100$ we reach the observed frequencies $f = 30$ and $f = 28$ Hz for a magnetic field strength of $B_{15} < 1$.

To summarize the findings of this section, we see a significant increase in the frequency of the magneto-elastic generalization of the crustal shear modes with increasing magnetic field strength. The details of this increase, like the dependence on the magnetic field strength or the spatial structure of the resulting QPOs, depend on the particular magnetic field configuration. For higher multipoles we find a weaker increase of the QPO frequencies with
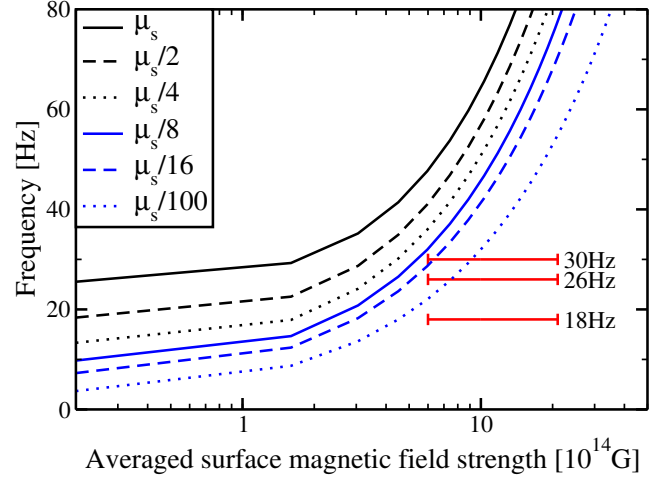
Figure 16. Extrapolation of the QPO frequencies using Eq. (34) for different values of the shear modulus μ_s in the presence of a dipole-like magnetic field for the QPO with $l' = 2$. The red lines indicate the lowest observed frequencies of the QPOs for the range of magnetic field strengths obtained using spin-down estimates for the three magnetars showing giant flares ($B_{15} = 0.6 \ldots 2.1$, see http://www.physics.mcgill.ca/~pulsar/magnetar/main.html).

the magnetic field strength than for dipole-like fields (see Fig. 15). However, the estimate of the magnetic field strength with the spin-down formula gives a lower estimate on the dipole-like component of the magnetic field. Therefore, the results of this section can be seen as providing a lower estimate of the frequency increase if there are additional multipoles present in the magnetic field structure. At surface field strengths of $B_{15} \sim 1$, expected from the spin-down estimates, the frequencies of the crustal shear modes are shifted to such high values that it is difficult to explain the lowest frequencies of the QPOs observed in SGRs even for strongly reduced shear moduli.

This result shows that our simplified treatment of different effects of the EoS on the magneto-elastic oscillations is valid in the particular case of magnetic fields confined to the crust. The effect of the magnetic field is the dominant one. Even when changing the shear modulus by a factor of about 100, we barely reach the observed frequencies at $B \sim 10^{15}$ G. Any additional correction on the structure of the crust or a more realistic calculation of the shear modulus would have to change the shear mode frequencies by at least one order of magnitude in the absence of the magnetic field in order to obtain frequencies of $f \lesssim 30$ Hz in the presence of the field. Additionally, it is not clear whether there would still exist shear-like QPOs in this case, i.e. when the magnetic field is dominant[7].

5.4 Different equilibrium models

In addition to the APR+DH EoS used for all the results discussed so far in this paper, we have also investigated neutron star models of 1.4 solar masses obtained with the APR+NV, L+DH and L+NV EoS, respectively. For all three EoS we have performed simulations

---

[7] As we have discussed previously in this section, the shear-like QPOs decrease in amplitude with increasing magnetic field strength until they disappear completely. Decreasing the shear modulus by a factor of 100, we would expect from Fig. 15 that the shear-like QPOs disappear at $B \sim 10^{15}$ G.

l' (nodes along θ)	EoS	$B_{\rm crit}$ [10^{14} G]	$b_{l'}$
2	APRDH	2.5	1.35
2	APRNV	3.6	1.69
2	LDH	2.3	1.46
2	LNV	3.5	1.59
3	APRDH	4.1	1.35
3	APRNV	5.3	1.49
3	LDH	3.4	1.36
3	LNV	5.2	1.48
4	APRDH	4.3	1.33
4	APRNV	5.6	1.45
4	LDH	3.8	1.37
4	LNV	5.8	1.47
5	APRDH	4.6	1.22
5	APRNV	6.0	1.41
5	LDH	4.1	1.27
5	LNV	6.0	1.39

Table 5. Parameters $B_{\rm crit}$ and $b_{l'}$ of Eq. (30) for a magnetic field configuration matched to an exterior dipole for different EoS and different number of nodes in θ-direction l', respectively.

at magnetic field strengths of $B_{15} = 0.1$, 0.5, 1.0, 2.0, and 5.0, respectively. As discussed in the previous section, it was highly problematic to identify the QPOs corresponding to the pure shear modes in the zero field limit for the strongest magnetic fields considered, because strong magnetic fields significantly change the QPOs. In particular those QPOs having a maximum at the equator ($l' = 3$ and $l' = 5$) are difficult to detect for the dipole-like field configuration. The Alfvén oscillations along the closed field lines in this region have very different structure and frequencies, and, thus, suppress shear-like oscillations.

The corresponding parameters $B_{\rm crit}$ and $b_{l'}$ for the fitting functions defined in Eq. (30) for $B_{15} \lesssim 1.5$ are given in Table 5 for the set of EoS and magnetic field amplitudes. There is a clear, albeit weak, dependence of the two parameters on the QPO structure characterized by l'. For low l' the critical magnetic field is weaker than for high l', and exactly the opposite holds for the exponent $b_{l'}$, which decreases with increasing l'. The influence of $B_{\rm crit}$ on the crustal EoS is of the same order of magnitude as the difference between different l'. The DH EoS leads to approximately 30% lower values of $B_{\rm crit}$ than the NV EoS. This strong effect of the magnetic field for models with the DH EoS can be easily understood because the NV EoS leads to models with larger shear moduli. The influence of the core EoS is less pronounced and one recovers very similar $B_{\rm crit}$ and $b_{l'}$ for the two examples studied here.

The dependence on the particular choice of the EoS is not very strong, and in all cases we find that the frequencies increase significantly starting at a few 10^{14} G. Therefore, for these configurations and all EoS analyzed, we cannot interpret the lowest observed QPO frequencies in terms of shear-like QPOs. Additionally, without the identification of the fundamental shear mode, it is not possible to explain the order of the higher frequency QPOs ($f > 30$ Hz) with shear modes. If the $l' = 2$ mode has a higher frequency of the order of the frequencies of the higher l' modes does not match with observations. Another possibility would be that the fundamental is not excited, but in this case one would have to explain why this happens.

6 COMPARISON WITH PREVIOUS WORK

Several authors have pointed out the possible existence of long-lived discrete crustal modes in the gaps between the Alfvén continua of the core (van Hoven & Levin (2011), Colaiuda & Kokkotas (2011), and van Hoven & Levin (2012)). None of the simulations of Gabler et al. (2011), Gabler et al. (2012), and the present work show this behavior. In Gabler et al. (2012) we performed a numerical experiment tailored to find these crustal modes to no avail. In Section 3.1.3 we presented new numerical simulations to test whether pure crustal shear oscillations can survive in the gaps of the Alfvén continuum. For this purpose we construct a particular model (F) with a flat spectrum which has large gaps in between successive overtones. In none of our simulations, however, we could find the crustal shear modes. Instead, coupled magneto-elastic oscillations of the continuum were present. In the following we compare these findings with those of previous work to understand the reason for the apparent discrepancy.

6.1 Comparison with Colaiuda & Kokkotas

Colaiuda & Kokkotas (2011) performed magneto-elastic simulations of axisymmetric torsional linear perturbations of magnetized neutron stars with a purely poloidal background field. They used tabulated EoS matching the core (Akmal et al. 1998, among others) with the crust (Negele & Vautherin 1973). This combination is very similar to APRDH that is used in the present work, and the same combination has been investigated in Gabler et al. (2012). Colaiuda & Kokkotas (2011) used a constant shear velocity in the crust that has a magnitude similar to the one used by us. They did not consider any effect due to superfluidity. Therefore, their results are directly comparable to those of Gabler et al. (2011), Gabler et al. (2012), and the present work (our work herafter).

The numerical simulations of Colaiuda & Kokkotas (2011) show that, even starting with pure perturbations of the crust, *the energy of the oscillations quickly flows from the crust towards the core exciting global oscillations*. They classify the oscillations as 'crustal modes', 'discrete Alfvén modes', and 'edges of the continuum'. The eigenfunctions of these oscillations (Figs. 3, 4, 6, 7 and 8 in Colaiuda & Kokkotas (2011)): (i) involve both crust and core, (ii) are confined to a limited range of magnetic field lines, and (iii) present nodes along the magnetic field lines but not across them. We also observe all three of these features in the oscillation patterns of all of our magneto-elastic QPOs, which indeed do not significantly differ from the modes described in Colaiuda & Kokkotas (2011) despite of their different naming. Therefore, we think that these oscillations correspond to excitations of the Alfén continuum.

6.2 Comparison with van Hoven & Levin

van Hoven & Levin (2012) performed simulations of the evolution of axisymmetric torsional oscillations. Their background model is similar to our magnetar models. They used a tabulated EoS comparable to that of our work, and the same prescription for the shear modulus. The background magnetic field is purely poloidal and corresponds to the configuration discussed in Section 3.1.4. However, the approach used by van Hoven & Levin (2012) to solve the magneto-elastic equations differs significantly from that in Colaiuda & Kokkotas (2011) and in our work. van Hoven & Levin (2012) construct a model for magnetar oscillation by coupling two sets of equations: one for the magneto-elastic oscillations of the crust, and another one for the Alfvén oscillations of the core. In

each region they search for an appropriate basis to expand the evolution equations. The basis in the core corresponds to the solution of the Sturm-Liouville problem for single magnetic field lines and zero displacement at the core-crust interface. In the *coupled case* it is necessary to introduce a new variable that is zero at the core-crust interface, because the displacement does not have to vanish there, in general. For the crust van Hoven & Levin (2012) choose the basis to be the set of discrete modes of the magnetized crust with zero-traction condition ($\xi^\varphi_{,r} = 0$) at the base of the crust. However, when the fully coupled system is considered, the displacement at the base of the crust is neither limited to be zero nor to have a zero radial derivative. Therefore, the fully consistent condition is not the zero traction condition, but the continuous traction condition $\xi^\varphi_{\mathrm{core},r} = \left[1 + \mu_\mathrm{S}/\Phi^4(b^r)^2\right]\xi^\varphi_{\mathrm{crust},r}$, i.e. we find that the basis used in the crust by van Hoven & Levin (2012) does not include all possible oscillations of the system, but only the subset fulfilling $\xi^\varphi_{,r} = 0$ at the core-crust interface. This effectively introduces a boundary condition at the core-crust interface which artificially reflects part of the magneto-elastic waves.

Due to the restrictions of their boundary treatment van Hoven & Levin (2012) neglect couplings between the crust and the core, in particular those involving crustal modes in the gaps of the continua, which do not show any interaction with the core in their simulations. van Hoven & Levin (2012) suggest that the discrepancy between their and our works could be related to the fact that they consider Alfvén waves coupling only to protons in the superfluid core while we do not. The effect of superfluidity on the magneto-elastic oscillations is beyond the scope of the present work and will be considered in future simulations to test whether crustal modes can occur in that case.

Actually, all QPOs of the different works discussed in this section scale more or less strongly with the magnetic field. Therefore, we prefer to call them magneto-elastic QPOs rather than crustal modes, because the latter expression gives the impression that the magnetic field does not influence the properties of these QPOs and the crustal modes can be obtained as in the field-free case, which is strictly not possible.

7   DISCUSSION

We studied the effect of different magnetic field configurations on the magneto-elastic oscillations of magnetars. For this purpose we have constructed magnetized equilibrium configurations generalizing the MAGSTAR routine of the LORENE library to include various descriptions of the current generating the magnetic field: MAGNETSTAR[8]. The oscillation spectrum, dominated by the continuum of the core, was studied by means of a semi-analytic model (Cerdá-Durán et al. 2009; Gabler et al. 2012) and numerical GRMHD simulations.

Table 6 summarizes the main results for the magnetic field configurations considered in this paper. For each model we identify the fundamental Alfvén QPO as the turning point in the Alfvén continuum at the lowest frequency. We identify this mode with some of the observed QPOs, the 30 Hz oscillation of SGR 1806-20 and 28 Hz of SGR 1900+1, and we estimate the *equivalent dipole magnetic field* strength of each configuration to match both frequencies. We define the *equivalent dipole magnetic field*, $\bar{B}$, as the magnetic

Model	QPO	$\bar{B}^{28Hz}_{15}$	$\bar{B}^{30Hz}_{15}$
A0	U1	2.1	2.3
$C_{0.1}$	U1	1.3	1.4
C_{10}	U1	2.1	2.2
A1	U1	3.1	3.3
A1	U2	2.1	2.3
O	U1	3.6	3.8
O	U2	1.9	2.0
F	U1	2.4	2.5
R_4	U1	1.1	1.2
R_4	U2	0.85	0.93
R_5	U1	1.5	1.6
R_5	U2	0.80	0.85
R_6	U1	2.0	2.1
R_7	U1	2.7	2.8
R_8	U1	3.5	3.8
$b_0 = 0$	U1	2.1	2.3
$b_0 = 1$	U1	2.2	2.4
$b_0 = 2$	U1	2.4	2.6
$b_0 = 5$	U1	2.9	3.1
$b_0 = 10$	U1	3.5	3.8
$b_0 = 20$	U1	3.7	4.0
Q/D=0.1	U1	2.1	2.2
Q/D=0.5	U1	2.5	2.7
Q/D=0.5	U2	3.5	3.7
Q/D=0.5	U3	1.5	1.6
Q/D=1.0	$U1_N$	0.93	0.99
Q/D=1.0	$U1_S$	4.0	4.3
Q/D=2.0	$U1_N$	0.53	0.57
Q/D=2.0	$U1_S$	0.87	0.93
Q/D=5.0	$U1_N$	0.24	0.25
Q/D=5.0	$U1_S$	0.28	0.30
Q/D=10.0	$U1_N$	0.12	0.13
Q/D=10.0	$U1_S$	0.13	0.14
Q	U1	0.076	0.081

Table 6. Equivalent field strength $\bar{B}$ to match the frequencies at $f = 28$ and $f = 30$ Hz with the QPO indicated in the table. $\bar{B}$ is defined by $m = \bar{B}R^3$ for a uniformly magnetized sphere, where m is the magnetic moment and R is the radius of the star. The QPOs Un_X are the Upper QPOs of the open field lines, n indicates the number of the corresponding turning points labelled from $n = 1$ at the polar axis to maximum $n = 3$ at larger θ, and X gives the division into northern ($X = N$) and southern ($X = S$) hemisphere, if there exist different QPOs in both hemispheres.

field strength at the surface of a Newtonian, uniformly magnetized sphere having the same dipole magnetic moment[9] m as the configuration we want to describe, which can be directly compared with the magnetic field estimates from spin-down measurements, through $\bar{B}[\mathrm{G}] > 3.2 \times 10^{19} \left(P[\mathrm{s}]\dot{P}\right)^{1/2}$ (Lorimer & Kramer 2004). Thus, the magnetic field estimates in Table 6 are directly comparable to estimates of the magnetic field from the spin down of the neutron star.

We summarize and discuss our main results next:

• For poloidal, purely dipole-like configurations generated by a toroidal current inside the star (type II) we observe that the Alfvén

---

[8] Our generalization of MAGSTAR is publicly available in the standard LORENE library.

[9] The value of m is provided in the output of the LORENE library, and the corresponding magnetic field strength can be computed from $m = \bar{B}R^3$. For the ring current m is given by $m = IA$, where I is the current and A the area of the current loop.

continuum always contains turning points at the polar axis (U1). Some models (A1, O, R_4, and R_5) have a second turning point (U2) in the region of open field lines inside the star. It seems very promising to identify some of the frequencies observed in the SGR giant flares, which are in the integer relation of 1:3:5 to each other[10], with the fundamental Alfvén Upper QPO at the polar axis and its second and fourth overtone. As can be seen in Table 6, the required equivalent field strength is in the range of 0.8 to 3.8×10^{15} G. This is consistent with the spin-down estimates of $\bar{B}_{15} > 2.4$ for SGR 1806-20 and $\bar{B}_{15} > 0.7$ for SGR 1900+14 (where $\bar{B}_{15}$ is $\bar{B}$ in units of 10^{15} G), respectively.

• The appearance of more than one turning point in the spectrum of some of the configurations allows us to relate additional observed frequencies to the torsional Alfvén oscillations. Model O was constructed such that we can match all frequencies observed in SGR 1900+14. It is possible to identify the 28 Hz with U1 at the polar axis, and the $84\,\text{Hz}= 3 \times 28\,\text{Hz}$ with its second overtone. Additionally, the 53 Hz QPO could be associated to U2 away from the polar axis at $\chi \sim 5\,\text{km}$ (see blue line in Fig. 2) and 155 Hz $\sim 3 \times 53\,\text{Hz}$ could be its second overtone. Interpreting the 30 Hz QPO of SGR 1806-20 as U2, and the 92 and 150 Hz ones as the second and fourth overtones, one could associate one of the lower frequencies, 18 or 26 Hz, with U1.

• We performed numerical simulations to test whether pure crustal shear oscillations can survive in the gaps of the Alfvén continuum, as it was proposed by van Hoven & Levin (2011). For this purpose we constructed a particular model (F) with a very flat spectrum which has very large gaps in between successive overtones. In none of our simulations we could find crustal shear modes. Instead, predominantly Alfvén oscillations of the continuum were present.

• For mixed poloidal-toroidal magnetic field configurations (type I) where the toroidal field is confined in the region of closed poloidal magnetic field lines inside the star, we estimate the part of the Alfvén spectrum of axial oscillations in the region of open field lines, where the toroidal component vanishes. Qualitatively, the spectrum is similar to the one of purely poloidal fields (type II) in that region. With increasing field strength of the toroidal component, the poloidal field strength near the closed field lines increases, too. This also means that the surface field becomes stronger. Table 6 (3rd set) shows the block for the different configurations b_0 we see that the necessary *equivalent dipole magnetic field* strength to match the observed QPO frequencies in the spectrum increases with increasing toroidal field, because of the stronger increase of the poloidal field strength close to the surface, while the field in the center is only mildly affected.

• Configurations with an additional quadrupole-like component have a richer spectrum when this component is of comparable strength as the dipole-like one. For $Q/D = 0.5$, we find three turning points in the spectrum. The additional turning points can produce oscillations which could be used to match a larger number of observed frequencies. For a quadrupole dominated configuration $Q/D \gtrsim 1.0$, we find asymmetric oscillations in both hemispheres of the neutron star. These provide a source for additional QPO frequencies which could be matched to observations. Models with $Q/D >> 1$, i.e. dominantly quadrupole-like configurations, are currently not favoured, since they require magnetic field strengths lower than standard spin-down estimates. The presence of a large quadrupole-like component in magnetars, comparable to the

poloidal component inside the star is not ruled out by our model. In fact the possible existence of this strong component could be related to the amplification of magnetic fields due to dynamo action, in initially rapidly rotating neutron stars in the standard magnetar formation scenario (Duncan & Thompson 1992). Once the dynamo stops, the magnetic field evolves mainly due to Hall drift (Goldreich & Reisenegger 1992) on a characteristic timescale

$$\tau_{\text{Hall}} = 5\,10^4 \left(\frac{L}{1\text{km}} \right) \left(\frac{10^{16}\text{G}}{B} \right) yr, \tag{35}$$

where B is the typical magnetic field strength in the magnetar interior, and L is the typical length scale of the magnetic field loops. Under such conditions, a quadrupole-like component of similar strength as the dipole-like one could still be present in magnetars, if it was present at birth.

• Finally, we investigated magnetic field configurations limited to the crustal region. These configurations could be realized if the neutron star core is a superconductor of type I. In this case the shear modes cannot be damped into the core of the neutron star and they might survive sufficiently long to become observable. However, our simulation results suggest that these models provide no viable explanation for the observed frequencies in SGRs. We showed that the influence of the magnetic field strength on the frequencies of the magneto-elastic QPOs can be cast into a semi-empiric formula, which also contains the effect of different shear moduli. With this relation, we are able to scan a wide range of parameters of magnetic field strength and magnitude of the shear modulus. The two possible types of QPOs are not favoured because: i) On one hand, the structure and in particular the frequencies of predominantly shear modes in the zero-magnetic-field case change significantly with increasing magnetic field, such that the lowest observed frequencies of $f \lesssim 30Hz$ cannot be reached for the currently expected values of the shear modulus and the magnetic field strength. ii) On the other hand, predominantly Alfvén oscillations will be quickly damped by phase mixing due to strong gradients in the spectra and an absence of turning points. For different EoS we obtain similar results. As expected, the core EoS does not play a large role in the determination of the critical magnetic field strength at which the frequencies begin to increase significantly with the magnetic field. The NV crust EoS leads to larger crusts with stronger shear moduli compared to the DH EoS. This, in turn, causes the necessary magnetic field to change the predominantly shear QPOs significantly to be up to 2×10^{14} G stronger than for the DH EoS. For quadrupole- or octupole-like dominated fields, the increase in frequencies of predominantly shear QPOs is less strong compared to dipole-like fields. However, from the neutron star spin-down measurement one has estimates of the dipole-like component of $B_{15} \sim 1$. At this dipole-like field strength our previous arguments already apply and the frequencies are shifted to $f \gtrsim 30$ Hz.

To summarize our findings, we have explored a large parameter space of possible magnetic field configurations of neutron stars. We discovered additional features, such as new turning points in the spectra for purely poloidal configurations, which have the potential to explain more of the observed QPO frequencies. Configurations with a toroidal component, which is confined to the closed poloidal field lines, have very similar spectra compared to those of purely poloidal fields. Furthermore, our results do not favour the assumption that the magnetic fields are confined to the crust.

Our magnetic field configurations do not include fields which have a toroidal component extending throughout the whole neutron star, which may be realized during a giant flare where strong

---

[10] 30, 92, and 150 Hz for SGR 1806-20, and 28, 84, and 155 Hz for SGR 1900+14

toroidal fields are expected in the exterior (Beloborodov 2009; Fernández & Thompson 2007; Nobili et al. 2008). For such configurations Colaiuda & Kokkotas (2012) find discrete Alfvén oscillations. However, these fields require currents at the surface of the neutron star, which are difficult to model (and are set ad hoc in other studies). We postpone such considerations to future work.

The origin of the high frequency QPOs with $f = 625$ Hz or higher remains open. In the magneto-elastic model the crustal $n = 1$ shear modes are damped less efficiently than the $n = 0$ modes, however, they still disappear on timescales much too short to be observable (Gabler et al. 2012; van Hoven & Levin 2011). One potential alternative solution of this problem is related to non-axisymmetric Alfvén oscillation of superfluid stars (Passamonti & Lander 2012). Also oscillations of the magnetospheric field may play a role at these high frequencies.

In a previous work (Gabler et al. 2012) we have studied the effect of different EoS for one particular magnetic field configuration. The differences in the estimated magnetic field strength required to match observations that are caused by changing the EoS are of the same order (factor of a few) as the differences caused by assuming different magnetic field configurations. One of the main open questions in order to match observations is the effect of superfluidity in the core of the neutron star, which probably leads to lower (and thus probably more realistic) estimates of the magnetic field strength (see Passamonti & Lander 2012, for recent progress on this topic). Furthermore, a model of how the coupling of the interior oscillations to the magnetosphere can lead to a modulation of the X-ray emission needs to be developed. We plan to address these two points in future studies.

APPENDIX A: MAGNETIC FIELD CONFIGURATIONS CONFINED TO THE CRUST

A more complete derivation of the following can be found in Aguilera et al. (2008). For axisymmetric fields it is possible to make the following ansatz

$$\mathbf{B}_{\text{poloidal}} = \boldsymbol{\nabla} \times (\mathbf{r} \times \boldsymbol{\nabla}\psi),\tag{A1}$$

where $\psi = \psi(r, \theta)$ is a scalar whose angular part can be expanded according to

$$\psi(r, \theta) = C \sum_l \frac{P_l(\cos\theta)}{r} S_l(r),\tag{A2}$$

with C being a normalization constant. The poloidal magnetic field can thus be expressed as

$$B_r = -\frac{B}{2x^2} S_l(x) \frac{1}{\sin\theta} \frac{\partial}{\partial\theta}\left(\sin\theta \frac{\partial}{\partial\theta} P_l(\cos\theta)\right),\tag{A3}$$

$$B_\theta = \frac{B}{2x}\frac{\partial}{\partial x}S_l(x)\frac{\partial}{\partial\theta}P_l(\cos\theta),\tag{A4}$$

where $x = r/r_{\text{s}}$ and B is a constant related to C. For dipolar fields $C = r_{\text{s}}^2 B/2$. The φ-component of the force-free condition $\boldsymbol{\nabla} \times \mathbf{B} = \mu\mathbf{B}$ leads to a Riccati-Bessel equation for $S_l(x)$ (see Aguilera et al. 2008). μ is a parameter related to the currents maintaining the magnetic field. For different l, we have

$$S_l(x) = a_l\mu r_{\text{s}} x\, j_l(\mu r_{\text{s}} x) + b_l\mu r_{\text{s}} x\, n_l(\mu r_{\text{s}} x),\tag{A5}$$

where a_l and b_l are parameters, and j_l and n_l are the spherical Bessel functions of first and second kind. The parameters a_l and b_l can be obtained by matching to an exterior solution of the magnetic field.

For a given l both have to be determined by the boundary conditions for B_r and B_θ at the surface. For a dipole external field we get

$$a_1 = \cos\mu r_{\text{s}},\tag{A6}$$

$$b_1 = \sin\mu r_{\text{s}},\tag{A7}$$

while for the quadrupole external field

$$a_2 = 3\frac{\sin\mu r_{\text{s}}}{(\mu r_{\text{s}})^2} - \sin\mu r_{\text{s}} - 2\frac{\cos\mu r_{\text{s}}}{(\mu r_{\text{s}})} + 3\frac{\cos\mu r_{\text{s}}}{(\mu r_{\text{s}})^3},\tag{A8}$$

$$b_2 = -3\frac{\cos\mu r_{\text{s}}}{(\mu r_{\text{s}})^2} + \cos\mu r_{\text{s}} - 2\frac{\sin\mu r_{\text{s}}}{(\mu r_{\text{s}})} + 3\frac{\sin\mu r_{\text{s}}}{(\mu r_{\text{s}})^3}.\tag{A9}$$

The octupole field can be matched by

$$a_3 = \cos\mu r_{\text{s}} - 5\frac{\sin\mu r_{\text{s}}}{\mu r_{\text{s}}} - 15\frac{\cos\mu r_{\text{s}}}{(\mu r_{\text{s}})^2} + 30\frac{\sin\mu r_{\text{s}}}{(\mu r_{\text{s}})^3}$$
$$+ 30\frac{\cos\mu r_{\text{s}}}{(\mu r_{\text{s}})^4},\tag{A10}$$

$$b_3 = \sin\mu r_{\text{s}} + 5\frac{\cos\mu r_{\text{s}}}{(\mu r_{\text{s}})} - 15\frac{\sin\mu r_{\text{s}}}{(\mu r_{\text{s}})^2} - 30\frac{\cos\mu r_{\text{s}}}{(\mu r_{\text{s}})^3}$$
$$+ 30\frac{\sin\mu r_{\text{s}}}{(\mu r_{\text{s}})^4}.\tag{A11}$$

It remains to determine the value of μ. For magnetic fields confined to the crust $B_r = 0$ at the crust-core interface. This translates into the condition $S_l|_{r_{\text{cc}}} = 0$, and hence for $l = 1$ into

$$\tan\left[\mu(r_{\text{cc}} - r_{\text{s}})\right] - \mu r_{\text{cc}} = 0,\tag{A12}$$

which has to be solved numerically. For the quadrupole- and octupole-like configurations the corresponding equations are more complicated and are not given here.

The particular form of $A(x)$ in general does not have to coincide with the solution in terms of spherical Bessel functions presented above. But because of arbitrariness it is advantageous to use an analytical description here.

REFERENCES

Aguilera D. N., Pons J. A., Miralles J. A., 2008, A&A, 486, 255
Akmal A., Pandharipande V. R., Ravenhall D. G., 1998, Phys. Rev. C, 58, 1804

Baym G., Pethick C., Pines D., 1969, Nature, 224, 673

Beloborodov A. M., 2009, ApJ, 703, 1044

Bocquet M., Bonazzola S., Gourgoulhon E., Novak J., 1995, A&A, 301, 757

Braithwaite J., Spruit H. C., 2006, A&A, 450, 1097

Cerdá-Durán P., Font J. A., Antón L., Müller E., 2008, A&A, 492, 937

Cerdá-Durán P., Stergioulas N., Font J. A., 2009, MNRAS, 397, 1607

Ciolfi R., Ferrari V., Gualtieri L., Pons J. A., 2009, MNRAS, 397, 913

Ciolfi R., Lander S. K., Manca G. M., Rezzolla L., 2011, ApJ, 736, L6+

Colaiuda A., Beyer H., Kokkotas K. D., 2009, MNRAS, 396, 1441

Colaiuda A., Ferrari V., Gualtieri L., Pons J. A., 2008, MNRAS, 385, 2080

Colaiuda A., Kokkotas K. D., 2011, MNRAS, 414, 3014

Colaiuda A., Kokkotas K. D., 2012, MNRAS, 423, 811

Douchin F., Haensel P., 2001, A&A, 380, 151

Duncan R. C., 1998, ApJ, 498, L45

Duncan R. C., Thompson C., 1992, ApJ, 392, L9

Fernández R., Thompson C., 2007, ApJ, 660, 615

Gabler M., Cerdá Durán P., Font J. A., Müller E., Stergioulas N., 2011, MNRAS, 410, L37

Gabler M., Cerdá-Durán P., Stergioulas N., Font J. A., Müller E., 2012, MNRAS, 421, 2054

Goldreich P., Reisenegger A., 1992, ApJ, 395, 250

Gourgoulhon E., 2012, 3+1 Formalism in General Relativity: Bases of Numerical Relativity. Springer (Berlin Heidelberg)

Israel G. L., Belloni T., Stella L., Rephaeli Y., Gruber D. E., Casella P., Dall'Osso S., Rea N., Persic M., Rothschild R. E., 2005, ApJ, 628, L53

Jackson J. D., 1998, Classical Electrodynamics, 3rd Edition. New York: Wiley

Kiuchi K., Kotake K., 2008, MNRAS, 385, 1327

Kiuchi K., Yoshida S., Shibata M., 2011, A&A, 532, A30+

Lander S. K., Andersson N., Glampedakis K., 2012, MNRAS, 419, 732

Lander S. K., Jones D. I., 2009, MNRAS, 395, 2162

Lander S. K., Jones D. I., 2011a, MNRAS, 412, 1394

Lander S. K., Jones D. I., 2011b, MNRAS, 412, 1730

Lander S. K., Jones D. I., 2012, MNRAS, 424, 482

Lasky P. D., Zink B., Kokkotas K. D., Glampedakis K., 2011, ApJ, 735, L20+

Levin Y., 2007, MNRAS, 377, 159

Lorimer D. R., Kramer M., 2004, Handbook of Pulsar Astronomy

Markey P., Tayler R. J., 1973, MNRAS, 163, 77

Negele J. W., Vautherin D., 1973, Nuclear Physics A, 207, 298

Nobili L., Turolla R., Zane S., 2008, MNRAS, 386, 1527

Page D., Prakash M., Lattimer J. M., Steiner A. W., 2011, Physical Review Letters, 106, 081101

Pandharipande V. R., Smith R. A., 1975, Physics Letters B, 59, 15

Passamonti A., Lander S. K., 2012, MNRAS, p. 347

Piro A. L., 2005, ApJ, 634, L153

Samuelsson L., Andersson N., 2007, MNRAS, 374, 256

Shternin P. S., Yakovlev D. G., Heinke C. O., Ho W. C. G., Patnaude D. J., 2011, MNRAS, 412, L108

Sotani H., Colaiuda A., Kokkotas K. D., 2008, MNRAS, 385, 2161

Sotani H., Kokkotas K. D., Stergioulas N., 2007, MNRAS, 375, 261

Sotani H., Kokkotas K. D., Stergioulas N., 2008, MNRAS, 385, L5

Steiner A. W., Watts A. L., 2009, Physical Review Letters, 103, 181101

Strohmayer T., van Horn H. M., Ogata S., Iyetomi H., Ichimaru S., 1991, ApJ, 375, 679

Strohmayer T. E., Watts A. L., 2005, ApJ, 632, L111

Tayler R. J., 1973, MNRAS, 161, 365

van Hoven M., Levin Y., 2011, MNRAS, 410, 1036

van Hoven M., Levin Y., 2012, MNRAS, 420, 3035

Watts A. L., Strohmayer T. E., 2007, Advances in Space Research, 40, 1446